Atmosphere–Ocean Momentum Exchange in General Circulation Models

JOHN A. T. BYE

School of Earth Sciences, The Flinders University of South Australia, Adelaide, South Australia, Australia

JÖRG-OLAF WOLFF

Antarctic CRC, Hobart, Tasmania, Australia

(Manuscript received 26 May 1997, in final form 24 April 1998)

ABSTRACT

A series of two-layer quasigeostrophic solutions for the ocean circulation driven by a steady wind in a channel with topography and in a flat bottom rectangular basin are presented in which the atmosphere and ocean are inertially coupled through the surface stress relation. The only other frictional processes are biharmonic lateral friction (under free-slip boundary conditions) and topographic form stress; there is no bottom friction involved. The results indicate that realistic momentum balances can be obtained on this physical basis. Two types of solutions are obtained, which are called (i) the I series in which the inertial coupling relation is applied directly in the earth reference frame with no current averaging and almost steady stream fields occur and (ii) the S series in which the inertial coupling relation is applied for long current averaging periods, of the order 100 days, rather than instantaneously. The solutions for the longer current averaging periods produce vigorous eddy fields, but their time-mean is very similar to the corresponding solution with no current averaging. Surface Stokes drift streamfields are also generated by the inertial coupling mechanism. Some implications of the results for general circulation modeling are discussed.

1. Introduction

The dynamical evolution of the circulation in the atmosphere and ocean depends strongly on property fluxes, like heat, momentum, and freshwater, at the sea surface. In general circulation models these fluxes are usually parameterized using bulk formulas, and therefore allow only a rather limited interaction between the two media. The growing interest in coupled ocean–atmosphere general circulation models for climate change studies has resulted in a renewed attention to the actual physics of the interaction between air and water. In particular, the role of surface gravity waves in the vertical transfer of momentum from air to ocean has been studied intensively in recent years (e.g., see Janssen 1989, 1991, 1992; Chalikov and Makin 1991; Weber 1994; Komen et al. 1994; Janssen and Viterbo 1996). It has been found that the surface stress and the resulting momentum transfer depend considerably on the sea state, with an enhanced transfer for ''rough'' young waves. These studies also showed that the momentum transfer between wind and waves could no longer be regarded as a one-way process but a two-way interaction (Janssen and Viterbo 1996). Recent coupled ocean–atmosphere model experiments on relatively fine grid resolution, which included a sea-state-dependent momentum transfer, demonstrated very significant changes in localized low pressure centers and affected sensible heat flux, maximum rain fall, and surface kinetic energy (Doyle 1994) as well as high- and low-frequency variability in the global atmospheric circulation (Janssen and Viterbo 1996). Currently a European coupled atmosphere wave ocean model is under development, which will allow full interaction of an atmosphere model, an ocean model, and a wave propagation and generation spectral model (Weisse 1997, personal communication) to study nontrivial interactions between waves and currents and wave-induced modifications of air–sea fluxes. This paper addresses the more fundamental aspects of interaction of two rotating fluids with large density contrast (inertial coupling) and proposes a new formulation of the surface shear stress for use in general circulation models.

The paper is organized as follows. The next section presents the novel aerodynamic bulk relationships, which take account of the wavefield. Section 3 discusses scales and procedures for implementing the inertial coupling relation in ocean general circulation models, and section 4 describes the formulation of the quasigeo-

Corresponding author address: Dr. John A. T. Bye, School of Earth Sciences, The Flinders University of South Australia, G.P.O. Box 2100, Adelaide, South Australia, 5001, Australia.
E-mail: john.bye@flinders.edu.au

strophic model. In sections 5 and 6 we present numerical solutions for the two most important ocean circulation problems—a doubly connected zonal flow like the Antarctic Circumpolar Current and a double gyre circulation in a closed basin such as the North Atlantic Ocean—using the inertial coupling relation, and contrast the results with experiments using the traditional surface forcing and bottom friction. Section 7 is devoted to a discussion of the results, and section 8 gives some conclusions.

2. Specification of the surface shear stress

The coupling between atmosphere and ocean has been emphasized as one of the ''most urgent scientific problems requiring attention'' in the Intergovernmental Panel on Climate Change report on Global Change 1995 (IPCC 1995). An important aspect of this coupling is the accurate specification of the surface shear stress. Traditionally this process has been regarded as a refinement of wind data quality and coverage and of the bulk aerodynamic relation, which converts this information into a shear stress. Concerns have been expressed from time to time on the influence of waves in this process because normally OGCMs do not also incorporate a wave model. In the outcome, reliance is usually placed on a statistically averaged drag relation, which is believed to represent the momentum transfer occurring under average sea states on whatever timescale the model is run. A synthesis of contemporary ideas can be found in Jones and Toba (1999).

In this section we ask the question whether this process is adequate in principle or whether it is fundamentally flawed and should be replaced by a new formulation. The implications of the correct resolution of the question are far reaching in so far as the momentum transfers at the sea surface are of importance both to the ocean and the atmosphere. It is suggested that surface gravity waves must be central in the discussion as they are the interfacial roughness elements, and viscous coupling alone as introduced by Ekman (1905) has been found to be an inadequate description.

Inertial coupling

The novel momentum exchange mechanism between atmosphere and ocean, which will be tested, is that at the sea surface the shear stress is represented by the two bulk aerodynamic relationships (Bye 1995) that take account of the wavefield: in air,

$$\boldsymbol{\tau}_s = \rho_1 K|\mathbf{u}(z) - (\mathbf{u}_0 + \mathbf{u}_L)| \times (\mathbf{u}(z) - (\mathbf{u}_0 + \mathbf{u}_L)) \quad (1a)$$

and in water,

$$\boldsymbol{\tau}_s = \rho_2 K|(\mathbf{u}_0 + \epsilon\mathbf{u}_L) - \mathbf{u}(-z)| \times ((\mathbf{u}_0 + \epsilon\mathbf{u}_L) - \mathbf{u}(-z)) \quad (1b)$$

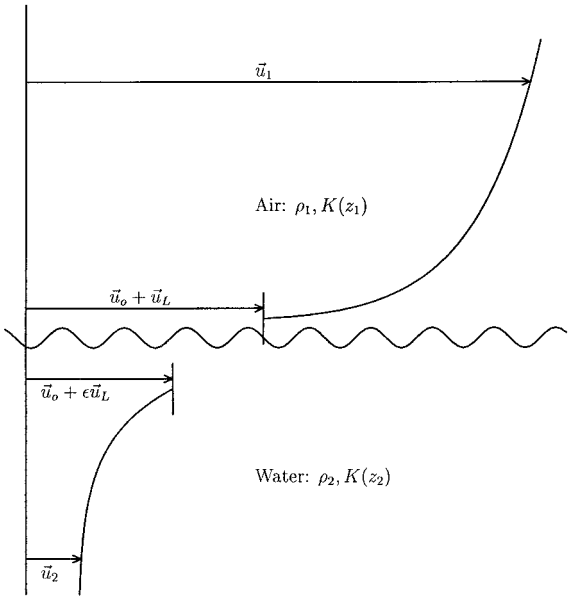

FIG. 1. Schematic of the inertial coupling concept: $\mathbf{u}_1$ is the air velocity, $\mathbf{u}_0$ is the reference velocity, $\mathbf{u}_L$ is the phase velocity, $\mathbf{u}_2 = \mathbf{U}_1$ is the water surface velocity (see Fig. 2), ρ_1 is the air density, ρ_2 is the water density, and $\epsilon = \sqrt{\rho_1/\rho_2}$ and $K(z_i)$ ($i = 1, 2$) are the drag coefficients in air and water, respectively.

in which $z = 0$ denotes the mean interfacial level; $\mathbf{u}$ is the fluid velocity; $\mathbf{u}_0$ is a non-wave-induced velocity, which will be called the reference velocity since it is common to both fluids; $\mathbf{u}_L$ is the spectrally averaged phase velocity of the wave spectrum; and $\epsilon\mathbf{u}_L$ is the spectrally integrated surface Stokes velocity, where $\epsilon = \sqrt{\rho_1/\rho_2}$, $K(\pm z)$ is a drag coefficient, ρ_1 and ρ_2 are respectively the densities of air and water, and $\boldsymbol{\tau}_s$ is the interfacial shear stress (Fig. 1). On equating (1a) and (1b) we obtain the inertial coupling relation (Bye 1995),

$$\boldsymbol{\tau}_s = \frac{1}{4}K|\rho_1^{1/2}(\mathbf{u}(z) - \mathbf{u}_0) - \rho_2^{1/2}(\mathbf{u}(-z) - \mathbf{u}_0)| \times [\rho_1^{1/2}(\mathbf{u}(z) - \mathbf{u}_0) - \rho_2^{1/2}(\mathbf{u}(-z) - \mathbf{u}_0)] \quad (2a)$$

and the auxiliary equation,

$$\mathbf{u}_0 = \frac{\epsilon\mathbf{u}(z) + \mathbf{u}(-z) - 2\epsilon\mathbf{u}_L}{1 + \epsilon}. \quad (2b)$$

The expressions (1a,b) and (2a,b) are assumed to apply within a wave boundary layer that extends upward and downward from the interface.

At the edges ($z = \pm z_B$) of the wave boundary layer the fluid velocity tends to the free-stream general circulation velocity, thus $\mathbf{u}_1 = \mathbf{u}(z_B)$ is the surface wind, and $\mathbf{u}_2 = \mathbf{u}(-z_B)$ is the surface current. In the following discussions the relations will be applied at these levels, except where mentioned otherwise.

On substituting (2b) in (2a) at the edge of the wave boundary layer, we obtain,

$$\boldsymbol{\tau}_s = \frac{\rho_1 K}{(1+\epsilon)^2}|\mathbf{u}_1 - \mathbf{u}_2 - (1-\epsilon)\mathbf{u}_L| \times (\mathbf{u}_1 - \mathbf{u}_2 - (1-\epsilon)\mathbf{u}_L). \quad (3)$$

Equation (3) is an explicit expression for $\boldsymbol{\tau}_s$ in terms of the free stream velocities in the two fluids and the two relevant spectrally integrated wave velocities. It indicates that the wave field causes a reduction in the surface stress when it is propagating with the wind and an increase in surface stress when it is propagating against the wind, and that wave effects are of *first order* importance since $\mathbf{u}_L = O(\mathbf{u}_1)$. For example, the surface Stokes drift for the wave spectrum for a fully developed sea is between 1.6% and 3.6% of the 19.5-m wind (Kenyon 1969), which would correspond with the range $0.5 \leq \mathbf{u}_L/\mathbf{u}_1 \leq 1.1$. In principle, it would be possible to use (3) to determine $\boldsymbol{\tau}_s$ and, since $\epsilon \ll 1$ and usually $|\mathbf{u}_2| \ll |\mathbf{u}_L|$ or $|\mathbf{u}_2| \ll |\mathbf{u}_1|$, this evaluation depends essentially only on the wind speed (u_1) and the spectrally integrated surface Stokes velocity (ϵu_L), which can be computed from the wave spectrum.

The statistically averaged drag coefficient K_1 expressed solely in terms of $\mathbf{u}_1$, using the classical formula,

$$\boldsymbol{\tau}_s = \rho_1 K_1 |\mathbf{u}_1| \mathbf{u}_1, \quad (4)$$

therefore has a site-specific relation between $\mathbf{u}_1$ and $\mathbf{u}_L$ built into it; for example, if the predominant winds blow over a shorter fetch, the drag coefficient would be expected to be greater than over larger fetch. In the open ocean, however, we have the concept of a fully developed sea in which a limiting relation is obtained between $\mathbf{u}_1$ and $\mathbf{u}_L$.

Within (3), however, lies a physical process not articulated in (4); that is, the wave spectrum, when it reduces the surface stress, is essentially returning momentum to the atmosphere. In the sense that the downward transfer of momentum across the sea surface is accomplished by the wind, it seems reasonable to suppose that any upward transfer must be due ultimately to the current.

The formal expression of this process (independent of the wavefield) is the inertial coupling relation (2a) in which the reference velocity $\mathbf{u}_0$ occurs in place of $\mathbf{u}_L$. Equation (2a) involves the turbulent shears in the two fluids, and the importance of that in water relative to air is weighted by the factor $1/\epsilon \approx 30$. The shear in water is a direct indication that a frictional drag exists on the surface current, analogous to that on the surface wind. Both shears can be measured, although the shear in the air is much easier to determine accurately, and a small error in estimating that in the water will cause a large error in the value of the shear stress. Nevertheless a complete wind–current–wave dataset should recover identical estimates of $\boldsymbol{\tau}_s$ by wave or shear measurements.

Equation (2a), however, points to a more fundamental factor in the discussion. The aerodynamic drag law is derived in a local coordinate system in which the non wave velocities are measured relative to the reference velocity ($\mathbf{u}_0$) such that the relevant velocities are ($\mathbf{u}_1 - \mathbf{u}_0$) and ($\mathbf{u}_2 - \mathbf{u}_0$). The numerical models, on the other hand, are not formulated in a local reference frame but in the reference frame of the solid body rotation of the earth.

3. The application of the inertial coupling relation in ocean general circulation models

The discussion of section 2 suggests that the inertial coupling relation (2) should be applied in general circulation models in the earth reference frame in which $\mathbf{u}_0 = 0$. The basis for this hypothesis is examined in detail in the appendix. In summary, it is argued that the inertial coupling relation should be applied to the general circulation with a uniform reference velocity ($\mathbf{u}_0$), which in the earth reference frame is $\mathbf{u}_0 = 0$. In the earth reference frame we denote the shear stress by $\boldsymbol{\tau}_{s0}$. Its application requires the specification of the surface wind $\mathbf{u}_1$ and the surface current $\mathbf{u}_2$ and of the drag coefficient K_0, where K_0 is the drag coefficient in (1) applicable for $\mathbf{u}_0 = 0$, each of which is considered in this section.

a. Averaging scales

The unspecified element in the application of (2) is the scale of averaging, the importance of which has been recognized for over a century (Reynolds 1894). In the open ocean the averaging of the wind and current in the inertial coupling relation occurs on different timescales. The wavefield is a response to the dynamics on both scales. It responds to the previous nonlocal wind field, that is, the short period mean wind (typically ≈10 h). It is reasonable to suppose that the wavefield also responds to the previous nonlocal current field but on a very different scale of averaging, and since observations indicate that the mesoscale eddy field does not greatly effect the wavefield, this implies that it responds to the long period mean current (typically ≈100 days).

b. Iterative procedure

These considerations suggest the following procedure for the application of the inertial coupling relation in an OGCM. Evaluate (2a) at the edge of the wave boundary layer to yield

$$\epsilon \mathbf{u}_L = \frac{1}{2}(\epsilon \mathbf{u}_1(T_1) + \mathbf{u}_2(T_2)), \quad (5)$$

where $\mathbf{u}_1(T_1)$ and $\mathbf{u}_2(T_2)$ are, respectively, moving averages of the wind over the interval (T_1) and of the current over the interval (T_2), which are assumed to generate the surface Stokes drift, $\epsilon \mathbf{u}_L(x, y, t)$. Then using (5) we obtain expressions for the reference velocity,

$$\mathbf{u}_0(T_1, T_2) = \frac{(\mathbf{u}_2 - \mathbf{u}_2(T_2) + \epsilon\langle \mathbf{u}_1 - \mathbf{u}_1(T_1)\rangle)}{1+\epsilon}, \quad (6)$$

and for the shear stress in the earth reference frame

$$\boldsymbol{\tau}_{s0}(T_1, T_2) = \frac{\rho_1 K_I}{(1+\epsilon)^2} \times \left| \langle (2\mathbf{u}_1 - \mathbf{u}_1(T_1)) + \epsilon \mathbf{u}_1(T_1) \rangle - \left\langle (2\mathbf{u}_2 - \mathbf{u}_2(T_2)) + \frac{\mathbf{u}_2(T_2)}{\epsilon} \right\rangle \right| \times \left(\langle (2\mathbf{u}_1 - \mathbf{u}_1(T_1)) + \epsilon \mathbf{u}_1(T_1) \rangle - \left\langle (2\mathbf{u}_2 - \mathbf{u}_2(T_2)) + \frac{\mathbf{u}_2(T_2)}{\epsilon} \right\rangle \right), \quad (7)$$

where $K_I = \frac{1}{4}K_0(\pm z_B)$. Here, $\boldsymbol{\tau}_{s0}(T_1, T_2)$ is the shear stress used in the simulations in which T_1 and T_2 are specified. The shear stresses, $\boldsymbol{\tau}_{s0}(t_1, t_2)$ over shorter averaging intervals (t_1, t_2), in the range $\Delta t \le t_1 \le T_1$ and $\Delta t \le t_2 \le T_2$, where Δt is the timestep of the model, may be also evaluated from the solutions. In the following discussion, we denote $\boldsymbol{\tau}_{s0}(T_1, T_2)$ by $\hat{\boldsymbol{\tau}}_{s0}$ and $\boldsymbol{\tau}_{s0}(\Delta t, \Delta t) \equiv \boldsymbol{\tau}_{s0}$ where

$$\boldsymbol{\tau}_{s0} = K_I |\rho_1^{1/2}\mathbf{u}_1 - \rho_2^{1/2}\mathbf{u}_2|(\rho_1^{1/2}\mathbf{u}_1 - \rho_2^{1/2}\mathbf{u}_2); \quad (8)$$

$\hat{\boldsymbol{\tau}}_{s0}$ can be regarded as the shear stress pertaining to the largest timescale of horizontal motion and $\boldsymbol{\tau}_{s0}$ to the smallest scale. An important property of (6) is that for instantaneous velocities that are equal to their respective moving average values,

$$\mathbf{u}_0(T_1, T_2) = 0 \quad (9)$$

and

$$\boldsymbol{\tau}_{s0}(T_1, T_2) = K_I |\rho_1^{1/2}\mathbf{u}_1(T_1) - \rho_2^{1/2}\mathbf{u}_2(T_2)| \times (\rho_1^{1/2}\mathbf{u}_1(T_1) - \rho_2^{1/2}\mathbf{u}_2(T_2)). \quad (10)$$

c. Natural occurrence of the limit $\tau_s \to \tau_{s0}$

In order to obtain an accurate simulation, it is important to know only the drag coefficient K_0. The first question we ask is, when is the limit $\mathbf{u}_0 \to 0$, in which (2a) and (8) become identical, approached in nature? This question is easily addressed for conditions in which $\boldsymbol{\tau}_s$ and $\mathbf{u}_L$ are collinear so that the classical formula (4) is applicable by defining $R = (\epsilon \mathbf{u}_L)/\mathbf{u}_0$ and using (2). After some algebra, the following scalar equation for the surface shear stress is obtained:

$$\tau_s = \frac{\rho_1 K}{(1+\epsilon X)^2} |u_1 - X u_2|(u_1 - X u_2), \quad (11)$$

where

$$X = \frac{(1 + R/\epsilon)}{(1+R)}.$$

In (11), the weighting X of the surface current relative to the surface wind varies between 1 and $1/\epsilon$ ($\approx$30), as a function of R. For $R \to \infty$ it tends to the wave dominant limit in which $\boldsymbol{\tau}_s = \boldsymbol{\tau}_{s0}$. An important property is that R need not be very large for the wave dominant limit to be a good approximation, for example, for $R = 1$ in which the surface Stokes drift velocity and the surface reference velocity are equal, $X = 15.2$; hence good estimates of K_0 can be made in many commonly occurring situations.

In the wave dominant limit ($R \to \infty$) we assume that at the edge ($z = -z_B$) of the wave boundary layer $u(-z_B) = 0$, and hence from (1a), we directly obtain

$$K_0(\pm z_B) = \left(\frac{w_*}{\epsilon u_L} \right)^2, \quad (12)$$

where $w_* = \sqrt{\tau_s/\rho_2}$ is the water friction velocity, in which $\boldsymbol{\tau}_s = \boldsymbol{\tau}_{s0}$. From (12) the drag coefficient in (7), evaluated at the edge of the wave boundary layer (Bye 1996), is

$$K_I = \frac{1}{4}\left(\frac{\epsilon u_L}{w_*} \right)^{-2}. \quad (13)$$

This result relies only on the ratio of the surface Stokes drift current relative to the water friction velocity. Estimates of this quantity were obtained in Bye (1988), in which it was found that $\epsilon u_L/w_* \approx 12$ such that $K_I = 1.7 \times 10^{-3}$.

The important relationship for the large-scale modeler is the inertially coupled geostrophic relationship. A planetary boundary layer model is not presented here as the general circulation model results are of an exploratory nature. It is clear however that in a quasigeostrophic model a somewhat lower coupling coefficient should be used to couple the surface geostrophic velocities in the two fluids, since the surface geostrophic velocities are greater than their respective velocities at the edge of the wave boundary layer; also, a small rotation of the shear stress vector in the planetary boundary layer should be incorporated. In the solutions to be presented in sections 5 and 6, we adopt a simple model in which $\mathbf{u}_1$ and $\mathbf{u}_2$ are assumed to be the surface geostrophic velocities in air and water, respectively, and take account of the Ekman layer simply by reducing K_I, which is applicable at the edge of the wave boundary layer; that is, we neglect the effects of rotation. A model of the inertially coupled planetary boundary layers (Bye, unpublished manuscript) indicates that a constant reduction factor of 0.7 may be applied, giving a geostrophic coefficient of 1.2×10^{-3}. This value is used for K_I in the solutions. The notation for the quasigeostrophic model (section 4) is that normally used, in which 1 refers to the upper layer and 2 refers to the

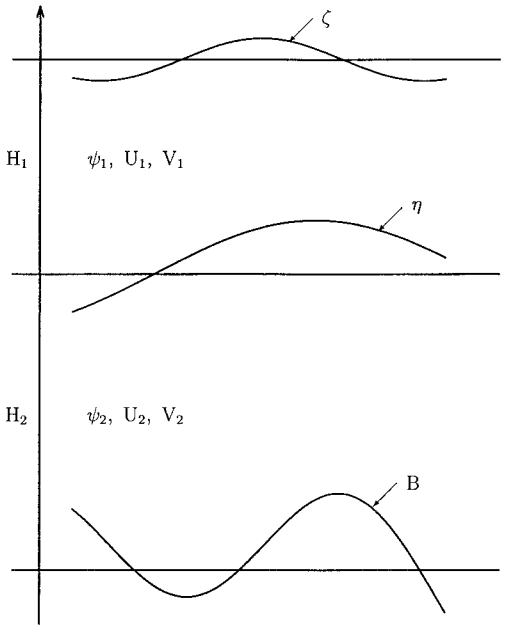

FIG. 2. Schematic of the two-layer quasigeostrophic model. Here, H_i ($i = 1, 2$) is the mean layer thicknesses, B the amplitude of the bottom topography anomaly, η the interface height, and ζ the sea surface height. Also, ψ_i is the velocity streamfunction in each layer, with U_i and V_i the corresponding eastward and northward velocities.

lower layer, and to avoid ambiguity we call the upper-layer geostrophic velocity $\mathbf{U}_1$ ($\equiv\mathbf{u}_2$) and the lower layer geostrophic velocity $\mathbf{U}_2$ (Fig. 2).

4. The model

The model used in this study is the one described in Wolff et al. (1991) with two modifications: First, a fourth-order accurate numerical discretization of the Jacobian operator (J_9) has been used as described in Wolff et al. (1993). This has only minor effects on lower order statistics like mean fields, momentum balance, and energy balance and has been introduced to compute higher order statistics like the eddy enstrophy balance for a study of eddy-flux parameterizations (Olbers et al. 1998, manuscript submitted to *J. Phys. Oceanogr.*; Ivchenko et al. 1997). Second, and more importantly for this study, the formulation of the frictional stresses at the sea surface has been changed as described further below. The model is based on quasigeostrophic dynamics and reflects the assumption of a rotating (β plane), hydrostatic, adiabatic fluid with two immiscible layers of different densities. The mean layer thicknesses are H_1 (1000 m) for the upper layer and H_2 (4000 m) for the lower layer. Two dynamically distinct situations of oceanic flow have been considered: a zonal reentrant channel of length X (4000 km) and width Y (1500 km), resembling the Antarctic Circumpolar Current, and a rectangular basin of length X (2560 km) and width Y (2560 km), resembling the western boundary current/gyral circulation in a Northern Hemisphere ocean basin. The model is eddy resolving with $\Delta x = \Delta y = 20$ km and a first baroclinic Rossby radius of 31.7 km for the channel centered at 60°S and 42.7 km for the rectangular basin centered at 40°N. The time step Δt is 2 h. The basic model equations are conservation equations for the potential vorticity q in each layer ($i = 1, 2$):

$$\frac{\partial}{\partial t}q_i + J(\psi_i, q_i) = F_i$$

with

$$q_i = H_i\nabla^2\psi_i + (-1)^i\frac{f_0^2}{g'}(\psi_1 - \psi_2) + fH_i,$$

where $g' = 0.02$ is the reduced gravity, f_0 is the Coriolis parameter at the reference latitude, the ψ_i represent the horizontal geostrophic velocity streamfunctions

$$U_i = -\frac{\partial}{\partial y}\psi_i$$

$$V_i = \frac{\partial}{\partial x}\psi_i,$$

and

$$F_i = \mathbf{k}\cdot\boldsymbol{\nabla}\times\boldsymbol{\tau}_i - A_4H_i\nabla^6\psi_i$$

summarize the curl of the frictional stresses acting on the fluid, which are surface stress $\boldsymbol{\tau}_1 = \hat{\boldsymbol{\tau}}_{s0}$, subgrid-scale lateral friction (biharmonic or hyperviscosity with $A_4 = 10^{10}$ m^4 s^{-1}), and linear bottom friction $\boldsymbol{\tau}_2 = -\epsilon^* H_2\mathbf{U}_2$. There is no momentum sink at the lateral walls due to a free-slip dynamic boundary condition. The kinematic boundary conditions on the sidewalls are $\psi_i = \text{const}$, which result in four different boundary values in the channel layout and two boundary values in the basin. The geometry of a reentrant channel represents a multiply connected area with an inner island and four auxiliary conditions are required to determine the values of the streamfunctions on the boundaries (only two of these conditions are needed for the basin geometry). These auxiliary conditions are based on mass conservation and an arbitrary normalization of the barotropic streamfunction on the boundaries for the basin, and for the channel geometry two additional auxiliary conditions based on the zonal momentum equations along the southern boundary are used according to McWilliams (1977). Numerically the solutions are obtained using second-order finite difference methods (besides the fourth-order treatment of the nonlinear advection term) and a three time-level leapfrog scheme as described in McWilliams et al. (1978), Wolff (1990), Wolff et al. (1991), and Olbers et al. (1998, manuscript submitted to *J. Phys. Oceanogr.*) for the channel experiments and Holland (1978) for the basin experiments.

We compare here experiments that differ in the formulation of the frictional stresses with the central experiments, FB (flat bottom channel) and M1 (channel

TABLE 1. Description of different experiments.

Case	Comments
FBI	Flat bottom reentrant channel (I series solution); see section 5a
FBS	as FBI but with 10–200 day current averaging (S series solution)
MCQI	Macquarie Ridge Complex Topography (see Fig. 5); (I series solution); see section 5b
MCQS30	as MCQI but with 30-day current averaging (S series solution); see section 6b(1)
MCQS300	as MCQI but with 300-day current averaging (S series solution); see section 6b(2)
DGI	Rectangular basin (double gyre, I series solution); see section 5c
DGIBF	as DGI but with bottom friction ($\epsilon^* = 10^{-7}$ s^{-1})
DGBF	as DGI but with wind forcing and bottom friction as in Holland (1978)
DGS300	as DGI but with 300-day current averaging (S series solution); see section 6c

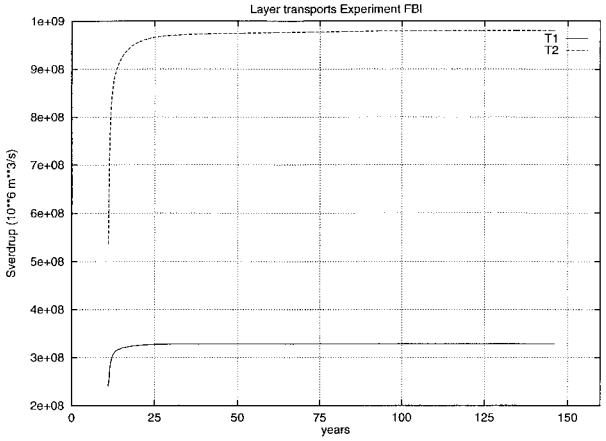

FIG. 3. Experiment FBI. Time evolution of volume transports in the upper layer (T1) and the lower layer (T2). Transport values in Sv ($\equiv 10^6$ m^3 s^{-1}). Time axis in units of years.

with Macquarie-Ridge-Complex topography), of Wolff et al. (1991). The rectangular basin solutions are discussed with reference to a similar experiment of Holland (1978). Table 1 gives an overview of the numerical experiments discussed in this paper. A steady wind field for which $\mathbf{u}_1(T_1) = \mathbf{u}_1$ was used throughout and two series of experiments were conducted. In the I series no current averaging was applied such that $\mathbf{u}_2(T_2) = \mathbf{u}_2$, $T_2 = \Delta t$ and $\hat{\boldsymbol{\tau}}_{s0} = \boldsymbol{\tau}_{s0}$, and in the S series the current averaging period (T_2) was gradually increased. The results for 30-day (S30) and 300-day current averages (S300) are presented in detail.

Inertial surface stress coupling

The surface stress in the following experiments varies in time and space as described above and consists of two components: a constant air velocity and a density-weighted upper-ocean velocity. To allow for a direct comparison with the original experiments in Wolff et al. (1991) and Holland (1978), the air velocity $\boldsymbol{u}_1$ has been diagnosed from the surface stresses in these papers using the bulk aerodynamic relation (4) with a constant drag coefficient $K_I = 1.2 \times 10^{-3}$:

$$\mathbf{u}_1 = \left(\sqrt{\frac{\tau^*}{\rho_1 K_I}}, 0\right) \tag{14}$$

with

$$\tau^* = \tau_0 \sin\left(\frac{\pi y}{Y}\right)$$

for the channel experiments and

$$\tau^* = -\tau_0 \cos\left(\frac{\pi y}{2Y}\right)$$

for the double-gyre basin experiments in which $\tau_0 =$ 0.1 N m^{-2}. The stress imparted on the ocean is now a function of the instantaneous (or time averaged) horizontal momentum of the upper ocean where

$$\mathbf{u}_2(T_2) \equiv \mathbf{U}_1(T_2) = \left(-\frac{\partial}{\partial y}\psi_1, \frac{\partial}{\partial x}\psi_1\right)(T_2).$$

The values of the streamfunction are taken at the central time level of the leapfrog scheme for $T_2 = \Delta t$ and represent a moving average over the timescale (T_2) otherwise.

5. The I series (solutions with no current averaging)

Three I series experiments, (1) a flat bottom channel, (2) a channel with topography, and (3) a flat bottom rectangular basin, will be discussed and compared with previous work that has used bottom friction.

a. Flat bottom channel (FBI)

The flat-bottom experiment with inertial surface stress coupling and zero bottom friction was started from a restart point of the topographic experiment with a Gaussian hill; see section 5b. The state of the circulation at this point was fully turbulent. The model was integrated for about 140 years (Fig. 3) and very rapidly evolved into a smooth laminar flow with time-mean transports of 329 and 980 Sv (Sv $\equiv 10^6$ m^3 s^{-1}) for the upper and lower layer, respectively. In this case the upper-layer transport can be computed analytically, that is, the stress free condition $\mathbf{u}_1 = \epsilon\mathbf{u}_2$ results in a total upper layer transport of

$$\int_0^Y H_1 U_1 \, dy = \frac{H_1 \epsilon Y \sqrt{\tau_0}}{\pi\sqrt{\rho_1 K_I}} \frac{\Gamma(3/4)\Gamma(1/2)}{\Gamma(5/4)}$$

in which $U_1 \equiv u_2$ (see section 3c), and the integral of

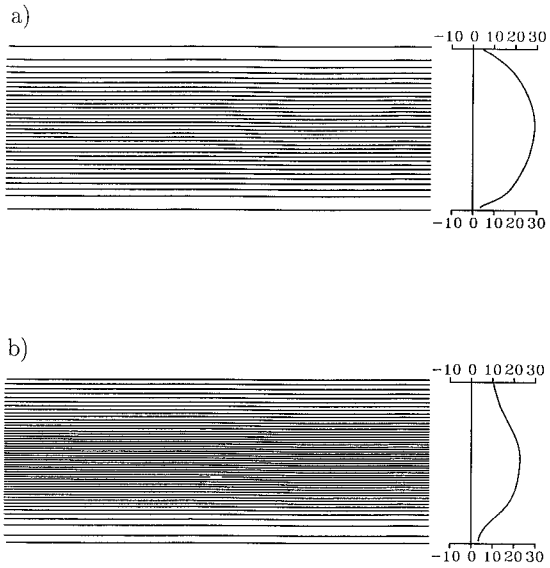

FIG. 4. Time mean streamfunctions of experiment FBI: (a) upper layer CI = 10^4 m^2 s^{-1} and (b) lower layer CI = 5×10^3 m^2 s^{-1}. The zonally averaged time-mean velocity as a function of latitude is indicated to the right of each panel. Units are centimeter per second.

the square root of the sine has been expressed with the aid of

$$\int_0^{\pi/2} \sin^{2\alpha+1}x \cos^{2\beta+1}x \, dx = \frac{\Gamma(\alpha + 1)\Gamma(\beta + 1)}{2\Gamma(\alpha + \beta + 2)}$$

and gives a value of about 330 Sv (for tables for the Γ function see, e.g., Abramowitz and Stegun 1972). The laminar streamfields (Wolff and Bye 1996) are shown in Fig. 4. The upper-layer mean zonal velocity mirrors the sinusoidal structure of the air velocity ($\sim\sqrt{\sin}$), and there is no momentum convergence into a jet. At the end of this run both fluids (air and water) are in inertial equilibrium in which the surface stress is zero, and no other forces are acting. With respect to the necessary condition for baroclinic instability in the two-layer model (e.g., see Kamenkovich et al. 1986)

$$\frac{U_1 - U_2}{((\beta g' H_2)/f_0^2)} = \theta \geq 1,$$

we find that θ just slightly exceeds the value of 1 over most of the channel width, its basin-average value $[\theta] \approx 1$, and conclude that this solution is baroclinically neutrally stable.

We emphasize that this solution is a steady-state equilibrium as is evident from Fig. 3. It is quite different from the turbulent solutions obtained with bottom friction (Wolff et al. 1991), which contain a vigorous transient eddy field.

b. Channel with topography (MCQI)

Two types of topography were used, which are identical with those described in Wolff et al. (1991). The solutions for a topographic obstacle in the form of a Gaussian hill have been reported elsewhere (Wolff and Bye 1996; Bye and Wolff 1997) and indicate an almost steady circulation in which the transports in both the upper and lower layers pulsate in a quasiperiodic manner. These preliminary results indicated that it was quite possible to achieve a realistic momentum balance in the circumpolar channel using surface friction and form drag without the necessity for bottom friction.

The implementation of a more complex topography (Fig. 5), which represents the Macquarie Ridge, the Campbell Plateau, the South Indian Ridge, and the adjacent abyssal basins, suitably interpolated to be cyclically continuous (Wolff et al., 1991) yielded a more chaotic regime in which regular oscillations in transport did not occur (Fig. 6). The overall appearance of the fields, however, changed only slightly with time such that the time mean (Fig. 7) and instantaneous (Fig. 8) flow patterns were similar, especially in the upper layer. The momentum balance in each layer shows that the transient eddies are of much less dynamical importance than the standing eddies (Fig. 9). There is however a remarkable modulation of the surface shear stress due to the current, and its latitudinal variation is no longer smooth but comprises a series of plateaus and rises. This mesoscale pattern arises from the surface-layer current field (see Fig. 7) and the associated convergences and divergences of momentum due to the Reynolds stresses of the standing eddies. The interfacial stress is transmitted almost unchanged to the topography through the action of form drag since the total Reynolds stresses are very similar to those in the top layer only (Fig. 9).

c. Flat bottom rectangular basin (DGI, DGIBF, DGBF)

The double-gyre circulation produced by a subtropical and subpolar wind-stress curl in a flat bottom rectangular basin has received much attention over the years (e.g. Holland 1978; Rhines and Young 1982; Holland and Schmitz 1985; Marshall et al. 1988, Veronis 1996). We obtained first the time-mean circulation for frictional parameters similar to Holland (1978). The main difference between our simulation and the earlier work was that the dimensions of the basin were 2560×2560 km^2, instead of 1000×2000 km^2, and that in addition to bottom friction a biharmonic, instead of Laplacian, lateral diffusion of momentum was used. Figure 10 shows the time-mean circulation for the bottom frictional parameter, $\epsilon^* = 10^{-7}$ s^{-1}, which in the upper layer indicates that a central jet extends about halfway across the basin. Zonally extended gyres exist on either side of this jet, which are more restricted meridionally in the lower layer than in the upper layer. The transports in the upper and lower layer of each gyre (relative to the boundary) are 59 Sv and 64 Sv, respectively. The Sverdrup transport, on the other hand is 10π Sv ($\beta = 2 \times 10^{-11}$ m^{-1} s^{-1}). Hence the bottom friction solution shows

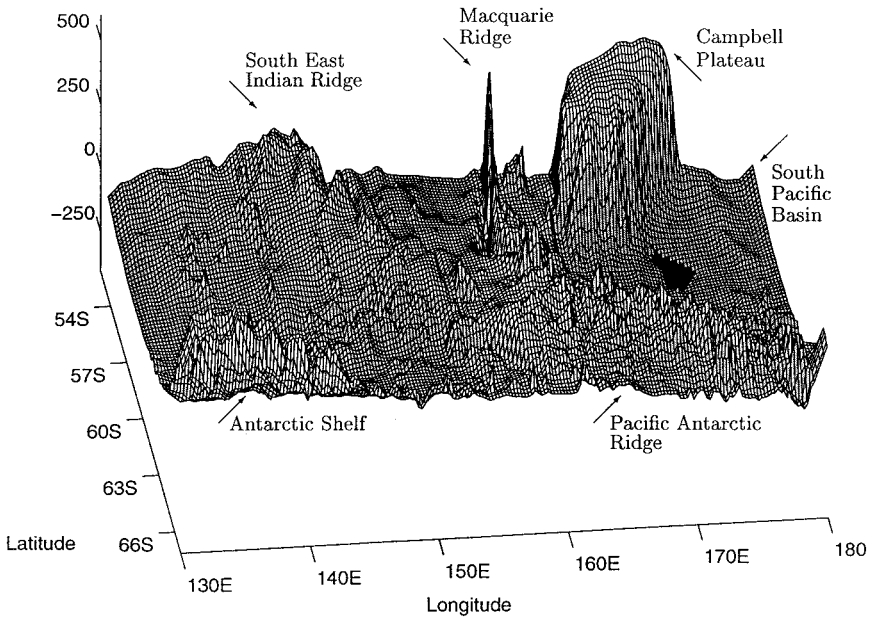

FIG. 5. Topography for the Macquarie Ridge Complex experiments (MCQ). The topography is rescaled to have a maximum amplitude of 500 m and a mean depth of 4000 m, to account for the restrictions of the quasigeostrophic approximation.

a strong enhancement of total transport over the inviscid Sverdrup limit. As we have pointed out in section 1, however, this value of the frictional parameter corresponds to an unrealistically large bottom current velocity, and it is anticipated that higher transports would be obtained for lower bottom frictional parameters.

The original solutions of Holland (1978) show similar enhancements of transport; for example, in his experiment 5, the upper-layer transport is 30 Sv and the lower-layer transport is 24 Sv, whereas in the smaller basin the inviscid Sverdrup transport is 5π Sv ($\beta = 2 \times 10^{-11}$ m^{-1} s^{-1}). Some other experiments (not shown here) indicate that very similar results are obtained with Holland's geometry and the lateral diffusion scheme used in our model.

The I series solution using (8) yields a circulation in the upper layer in which the zonal jet is more pronounced and the gyres on either side have a Sverdrup-

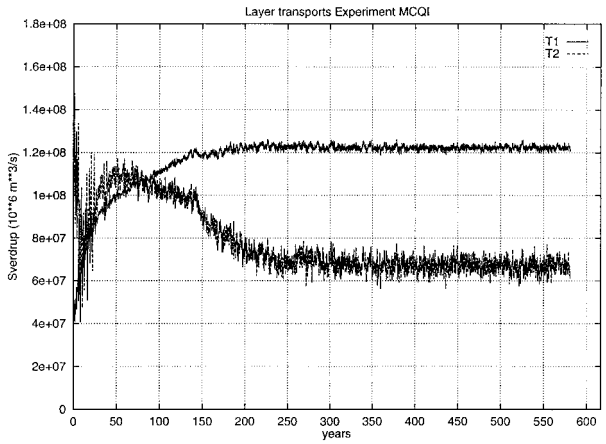

FIG. 6. Experiment MCQI. Time evolution of volume transports in the upper layer (T1) and the lower layer (T2). Transport values in Sv. Time axis in units of years.

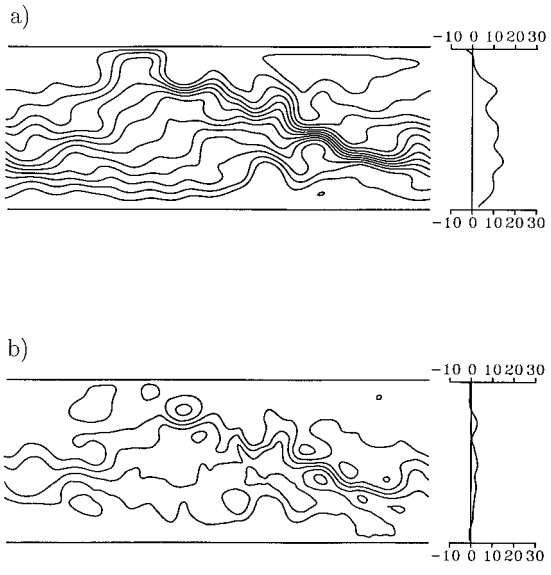

FIG. 7. Time-mean streamfunctions of experiment MCQI: (a) upper layer CI = 10^4 m^2 s^{-1} and (b) lower layer CI = 5×10^3 m^2 s^{-1}. The zonally averaged time-mean velocity as a function of latitude is indicated to the right of each panel. Units are centimeters per second.

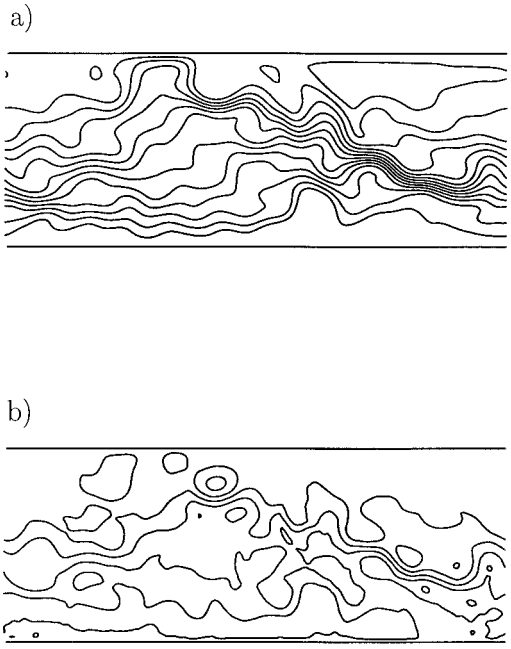

FIG. 8. Instantaneous streamfunctions of experiment MCQI at the end of the integration: (a) upper layer CI = 10^4 m^2 s^{-1} and (b) lower layer CI = 5×10^3 m^2 s^{-1}.

like character except for the inertial overshoots, which converge into the jet (Fig. 11a). An interesting feature is the sudden ending of the jet by a retroflection of the streamlines. In the lower layer (Fig. 11b) the recirculation is tightly focussed in comparison to the bottom friction solution, and its intensity, relative to the upper layer, surprisingly, is less. The transports are much smaller than the bottom friction transports and are 28 Sv in the upper layer and 5 Sv in the lower layer. Thus, the frictional reduction in transport (below the Sverdrup inviscid limit) is compensated almost exactly by an inertial increase. Another solution (DGIBF, not shown here) in which bottom friction ($\epsilon^* = 10^{-7}$ s^{-1}) was introduced into the simulation gave a very similar flowfield in the upper layer (28 Sv) and, as expected, a reduced transport in the lower layer (1 Sv).

We conclude from the experiments that: (i) the bottom friction mechanism is unable to reproduce a realistic gyral transport with a realistic gyral friction. This result complements a similar conclusion for the Antarctic Circumpolar Current (Wolff and Bye 1996). (ii) the upper layer I series solution is a robust result with respect to the influence of bottom friction, which reduces the lower layer transport but leaves the upper layer transport essentially unchanged.

The instantaneous flow patterns (Fig. 12) are similar to the time-mean patterns as in section 5b. A closer inspection shows that in the upper layer a series of wavelike perturbations are superimposed on the gyral streamlines (Fig. 12a). The cause of these waves is clear from the lower layer instantaneous field (Fig. 12b), which indicates a system of baroclinic Rossby waves propagating towards the west, until they are absorbed in the western boundary flow, and their momentum transfer gives rise to the interesting residual flow eddy pairs shown adjacent to the north and south boundaries in the time-mean lower layer circulation (Fig. 11b).

Figure 13 illustrates the energy balances that have settled to an almost steady-state balance in which the well-known dominance of the potential energy P over the kinetic energy K_i is evident. A small variability in P (presumably associated with the Rossby wave dynamics) is evident, and a notable feature is the extremely small kinetic energy in the lower layer (K_2).

d. Conclusion

The principal finding from the I series solutions is that realistic momentum balances can be obtained without using bottom friction, but this is at the expense of suppressing the transient eddy field. This finding is broadly consistent with the arguments of section 3c, which imply that the oceanic turbulence would be absent for $T_2 = \Delta t$. The I series solutions indicate that

$$\mathbf{u}_2 \sim \overline{\mathbf{u}}_2 \tag{15}$$

where $\mathbf{u}_2$ is the mean current. We conjecture that the dynamical reason for the absence of the transient eddy field is that the weighting of the surface current in (8), $\mathbf{u}_2/\epsilon$, is sufficient to make the flow baroclinically stable, whereas in the bottom-friction solution the flow is baroclinically unstable.

6. The S series (solutions with current averaging)

We present three sequences of S series solutions that correspond with the three I series solutions and incorporate moving current averages of different lengths.

a. Flat bottom channel (FBS)

The surface Stokes drift velocity obtained from the I series solution using (5), for all timescales of averaging of the surface current, is

$$\epsilon\mathbf{u}_L = \epsilon\mathbf{u}_1 = \mathbf{u}_2. \tag{16}$$

Thus, the wave model reduces to a wave field in which the surface Stokes drift velocity is everywhere equal to the surface ocean current, and the reference velocity is zero; that is, there is no shear in the wave boundary layer.

We always found this absolutely steady solution in our experiments [for current averaging times (T_2) from 10 days to 200 days]. Thus, it is concluded that, in the absence of perturbing forces, the coupled system tends to the steady equilibrium (16) in which the transient inertia resides totally in the surface wave field and the mesoscale eddy field is absent.

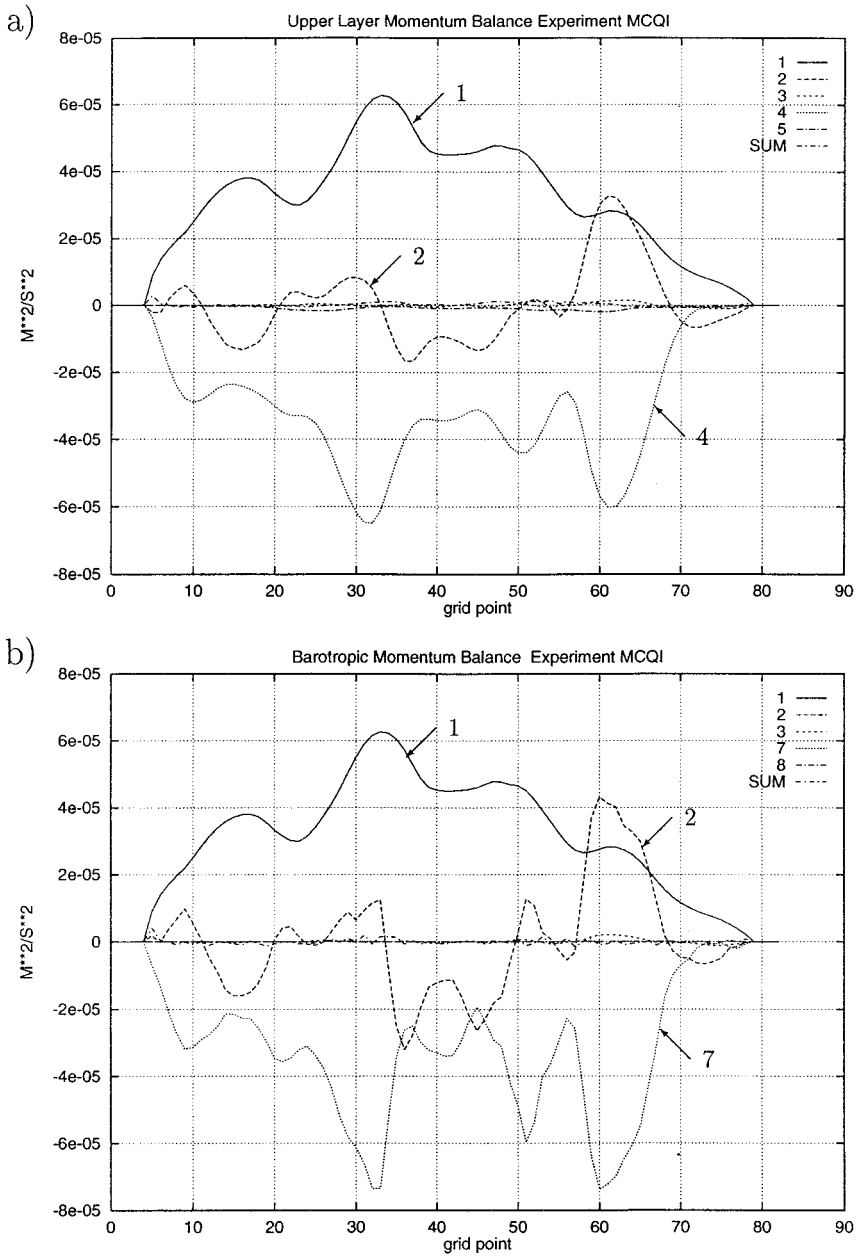

FIG. 9. Experiment MCQI: (a) upper layer momentum balance and (b) barotropic momentum balance. Contributing terms are surface stress (1), Reynolds stress divergence of the standing eddies (2) and transient eddies (3), interfacial form drag due to standing eddies (4) and transient eddies (5), topographic form stress (7), and bottom friction (8). Lateral friction effects (6) are negligible and therefore not displayed. Units are $m^2\ s^{-2}$. The northern and southern boundaries are located at grid points 4 and 79, respectively.

b. Channel with topography

The effect of topography is to perturb this equilibrium and to allow the possibility for a mesoscale eddy field to coexist with the wave field. A series of solutions was obtained in which the averaging time for the current in the computation of the surface Stokes velocity in (5) was increased. We illustrate the results using averaging periods of 30 and 300 days.

1) THE 30-DAY CURRENT AVERAGE (MCQS30)

The mean streamfields for the 30-day current average (Fig. 14) are very similar to those obtained in the so-

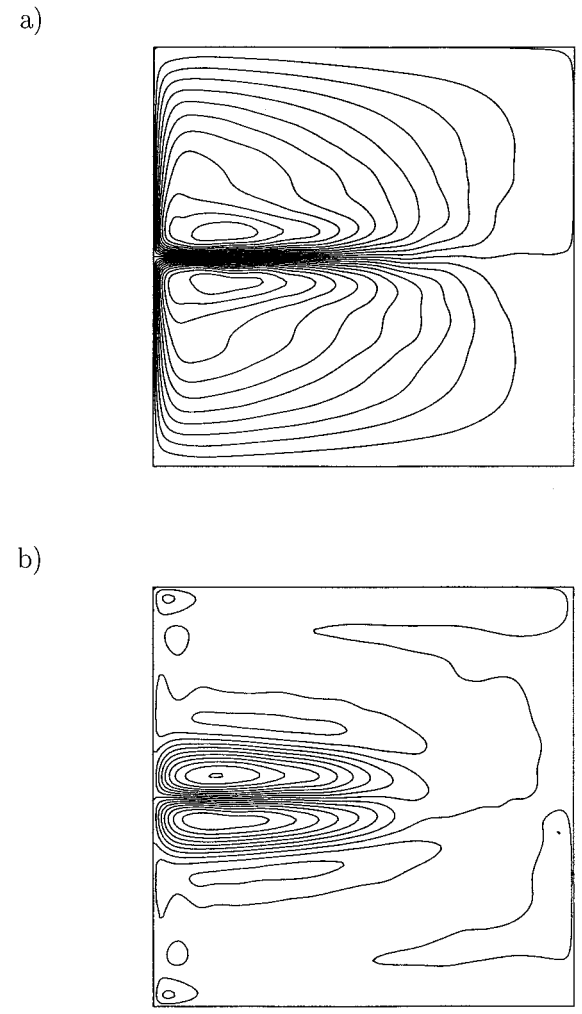

FIG. 10. Time-mean streamfunctions of experiment DGBF: (a) upper layer CI = 10×10^3 m^2 s^{-1} and (b) lower layer CI = 2×10^3 m^2 s^{-1}.

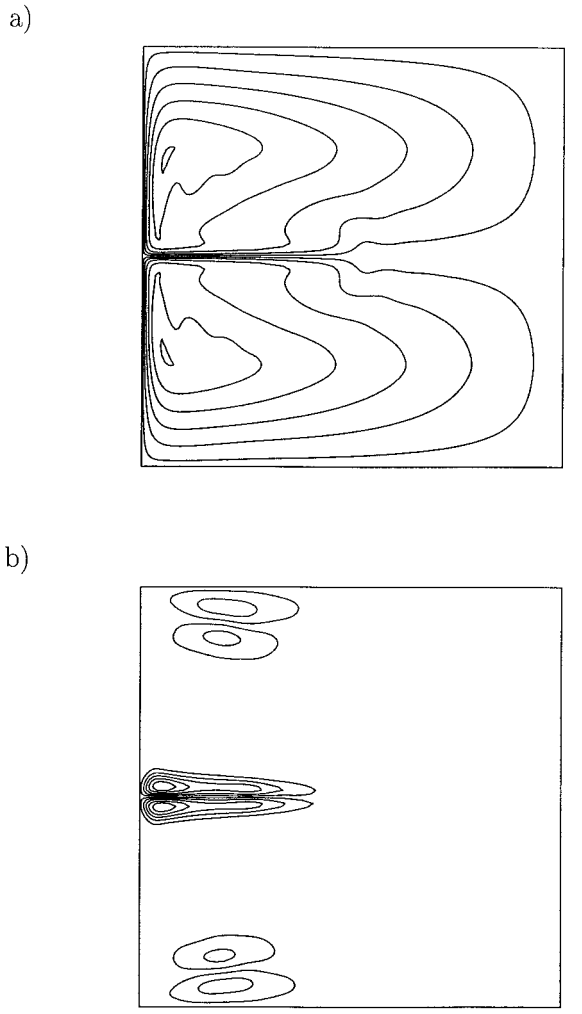

FIG. 11. Time-mean streamfunctions of experiment DGI: (a) upper layer CI = 5×10^3 m^2 s^{-1} and (b) lower layer CI = 200 m^2 s^{-1}.

lution with no current averaging. This illustrates that for this timescale of averaging, the transient momentum would be still contained mainly in the surface wave field. An inspection of the instantaneous field shows that occasionally eddies appear to spawn from the almost stationary circulation. The reference velocity streamfunction (Fig. 15a) obtained from (6) indeed shows that a field of weak eddies (relative to the 30-day current average field) has been produced, particularly associated with the main jet. The 30-day average surface current field itself is almost steady; that is, $\mathbf{u}_2(T_2) \approx \mathbf{u}_2$, where $\mathbf{u}_2$ is the mean current.

In a similar manner by (5), the surface Stokes streamfunction (Fig. 15b) also is almost steady and shows a pattern in which the components due to the wind and current combine to yield a modulation in speed and direction of the overall eastward flow, which presents a filamental pattern. The momentum balance is very similar to the I series solution (Fig. 9).

2) The 300-day current average (MCQS300)

The mean streamfields for the 300-day current average (Fig. 16) show significant differences from the 30-day current average. In particular, in the upper layer, the proto–Antarctic Circumpolar Current has a jetlike appearance at all longitudes (Fig. 16a). In the lower layer (Fig. 16b) there has been a redistribution of momentum from the central region of the channel to the side boundaries where westward jets have formed. An intense anticyclonic gyre has developed over the Campbell Plateau.

The cause of the formation of westward flows was investigated in Wolff et al. (1991), where it was suggested that a westward topographic stress could be generated by the interaction of the lower-layer circulation with random topography on a β plane, as discussed in Holloway (1987). In our solution, their development is more accentuated due to the absence of bottom friction. In reality, these jets would be suppressed by two factors:

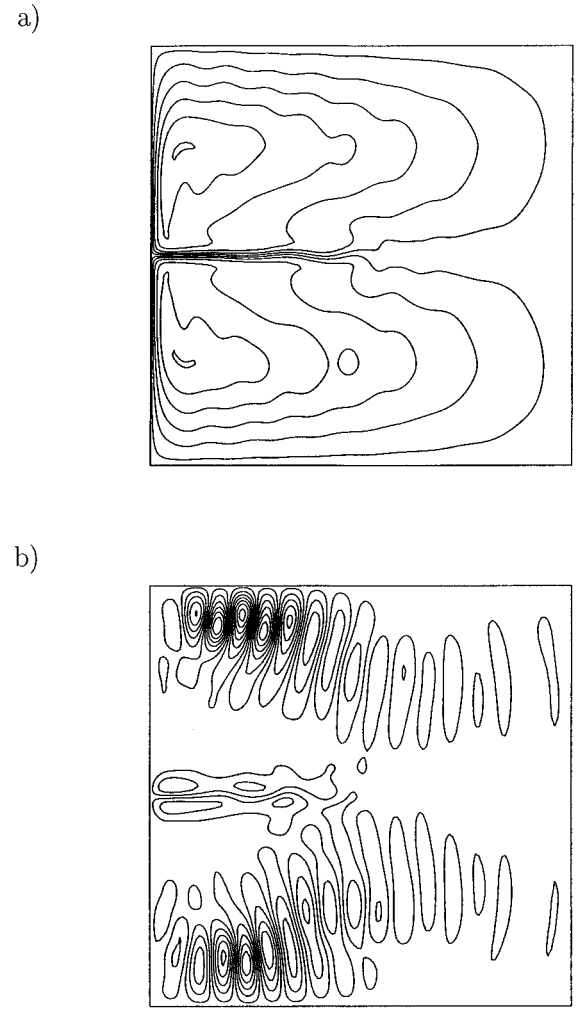

FIG. 12. Instantaneous streamfunctions of experiment DGI: (a) upper layer CI = 5×10^3 m^2 s^{-1} and (b) lower layer CI = 500 m^2 s^{-1}.

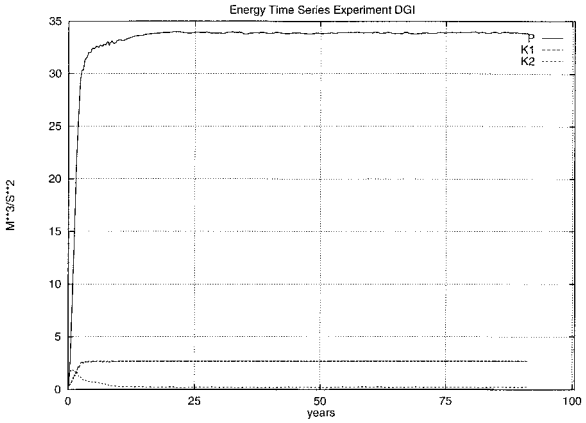

FIG. 13. Experiment DGI. Time evolution of potential energy (P) and layer kinetic energies (K_1, K_2). Energy values in m^3 s^{-2}. Time axis in units of years.

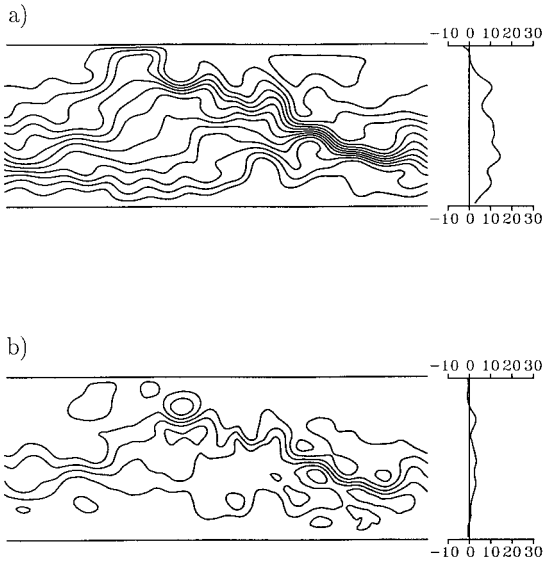

FIG. 14. Time-mean streamfunctions of experiment MCQS30: (a) upper layer CI = 10^4 m^2 s^{-1} and (b) lower layer CI = 5×10^3 m^2 s^{-1}. The zonally averaged time-mean velocity as a function of latitude is indicated to the right of each panel. Units are centimeters per second.

(i) leakage of momentum into the ocean basins from the circumpolar channel and (ii) the action of lateral and bottom frictional processes on the continental margins. The main focus here is the dynamics of the upper layer, which is controlled by the surface friction.

Instantaneous streamfunctions (Fig. 17) show that a

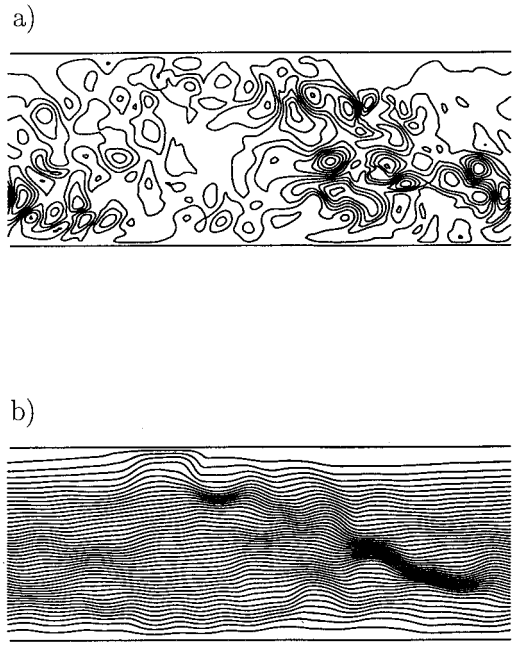

FIG. 15. Experiment MCQS30: (a) reference velocity streamfunction CI = 5×10^3 m^2 s^{-1} and (b) Stokes drift streamfunction CI = 5×10^3 m^2 s^{-1}.

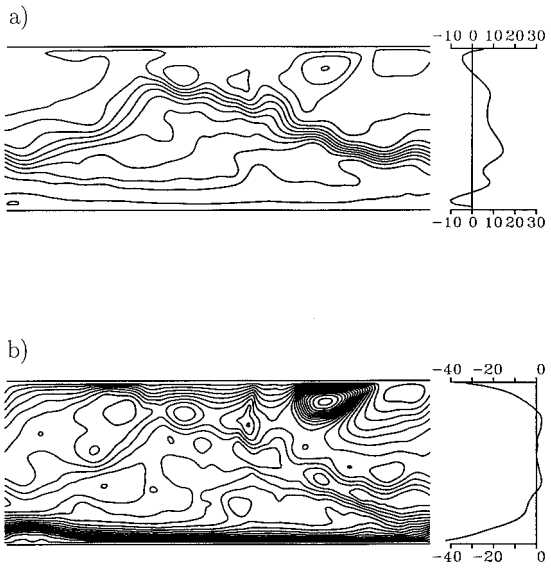

FIG. 16. Time-mean streamfunctions of experiment MCQS300: (a) upper layer CI = 10^4 m^2 s^{-1} and (b) lower layer CI = 5×10^3 m^2 s^{-1}. The zonally averaged time-mean velocity as a function of latitude is indicated to the right of each panel. Units are centimeters per second.

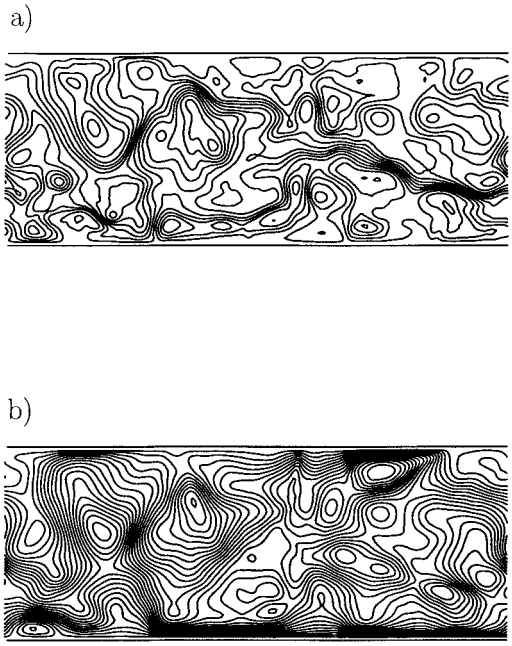

FIG. 17. Instantaneous streamfunctions of experiment MCQS300 at the end of the integration: (a) upper layer CI = 10^4 m^2 s^{-1} and (b) lower layer CI = 5×10^3 m^2 s^{-1}.

vigorous mesoscale eddy field exists in which both baroclinic and barotropic eddies are present. A notable feature is that the size of the transient eddies in the lower layer (Fig. 17b) is greater than in the upper layer (Fig. 17a), and a comparison with the mean field (Fig. 16) shows a high mean turbulent kinetic energy intensity,

$$[\xi] = \frac{[(\mathbf{u}_2 - \mathbf{u}_2(T_2))^2]}{[(\mathbf{u}_2(T_2))^2]},$$

in both layers, where $[\,\cdot\,]$ denotes a basin mean. In the upper layer, $[\xi] = 3.42$ and in the lower layer $[\xi] = 0.72$. These values contrast with $[\xi] = 0.03$ and $[\xi] = 0.04$, in the upper and lower layer, respectively, of the 30-day current average. The reference velocity streamfunction (Fig. 18a) shows a regular, almost homogeneous eddy field (relative to the 300-day current average) in contrast to that for the MCQS30 solution (Fig. 15a).

The instantaneous Stokes streamfunction (Fig. 18b) shows a circumpolar jet, which runs as a thread through the background streamfield produced by the surface wind. Another interesting feature is that the surface Stokes velocity is very weak adjacent to both boundaries, especially the southern boundary, due to the weak westward currents occurring in these locations. This cancellation of the components, however, may well be coincidence, arising from the atmospheric forcing and sidewall geometry of the model.

Using (8) and (7), the instantaneous surface shear fields $\boldsymbol{\tau}_{s0}$ and $\hat{\boldsymbol{\tau}}_{s0}$ have also been computed. The striking difference between the two fields (Fig. 19) is obvious: $\boldsymbol{\tau}_{s0}$ reflects the momentum exchange occurring between the atmosphere and ocean at the scale of resolution of the mesoscale eddies, which is the smallest scale of the resolved motion in the model and $\hat{\boldsymbol{\tau}}_{s0}$ is a prediction (using the wave model of the present analysis) of the surface shear stress, which acts on the largest scale of

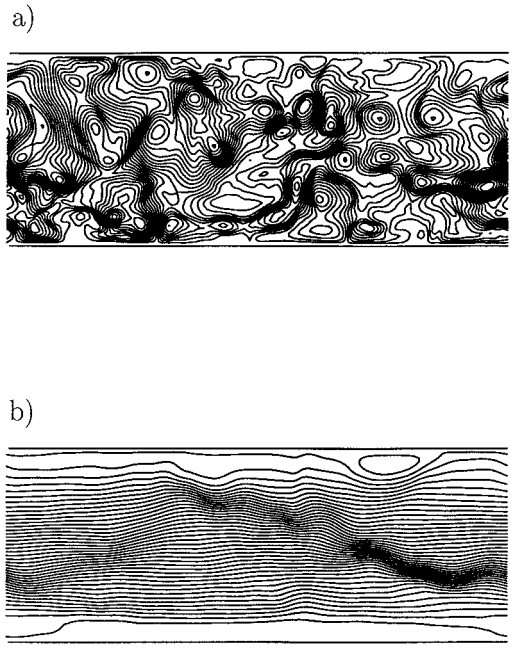

FIG. 18. Experiment MCQS300: (a) reference velocity streamfunction CI = 5×10^3 m^2 s^{-1} and (b) Stokes drift streamfunction CI = 5×10^3 m^2 s^{-1}.

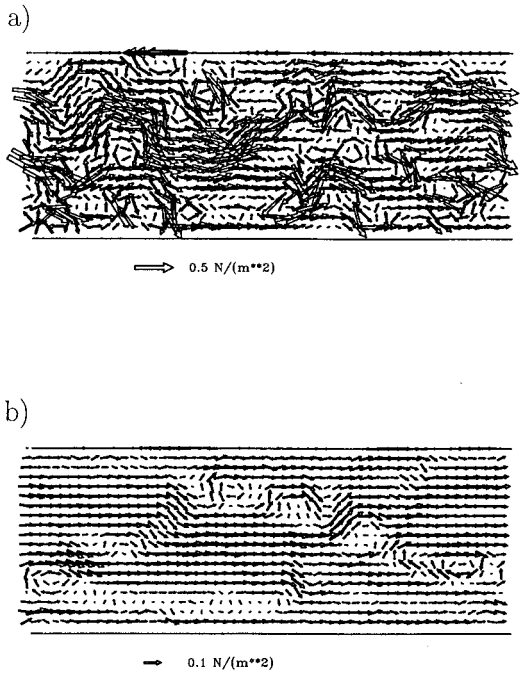

FIG. 19. Experiment MCQS300: (a) $\boldsymbol{\tau}_{s0}$ and (b) $\hat{\boldsymbol{\tau}}_{s0}$.

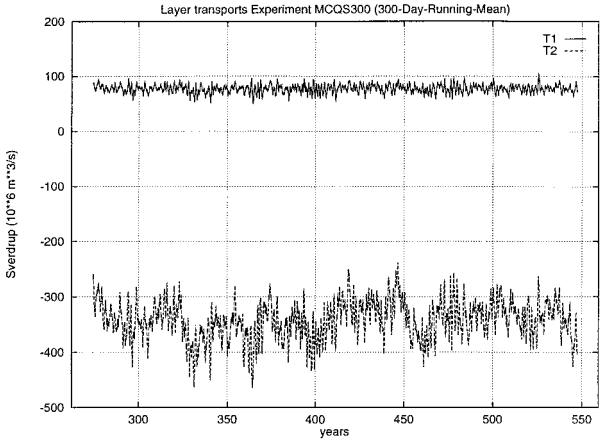

FIG. 20. Experiment MCQS300: time evolution of volume transports in the upper layer (T1) and the lower layer (T2) filtered with a 300-day moving average. Transport values in Sv. Time axis in units of years.

motion. The structure of $\hat{\boldsymbol{\tau}}_{s0}$ is related to the 300-day average surface current field and also to the applied zonal wind field. In the neighborhood of the circumpolar jet, both factors are of similar importance and give rise to the diagonal arrow patterns. In reality, it is anticipated that this structure would be relaxed somewhat since, in the fully coupled system, $\mathbf{u}_1(T_1)$ would adjust to the presence of the current. This conjecture remains to be tested in a coupled GCM.

The essential result, however, is that the Ekman transports on this scale (which are relevant to the study of mixing of water masses, oceanic fronts, and other global thermohaline phenomena) are very significantly affected by the surface current field. For example, the northward surface Ekman transport is partially arrested by the circumpolar jet, as can be seen from Fig. 19b.

We emphasize that both $\boldsymbol{\tau}_{s0}$ and $\hat{\boldsymbol{\tau}}_{s0}$ are instantaneous fields. The variability of the transport fields on a 300-day timescale (Fig. 20) shows a high-frequency response in both layers. The lower layer, in which the mean transport is -350 Sv due to the presence of the westward jets, also exhibits a vigorous low-frequency variability.

The momentum balance of the 300-day current average solution (MCQS300) differs greatly from the solution with no current averaging (MCQI) due to the presence of a more active eddy field. In the upper layer (Fig. 21a), the transient eddies now contribute to the momentum balance through Reynolds stress divergence and interfacial form stress. These transient contributions are of the same magnitude as the Reynolds stress divergence of the standing eddies in the inertial experiment. This momentum balance is similar to that obtained in the bottom-friction solution (M1 in Wolff et al. 1991) except for the very important feature that the surface stress profile (Fig. 21) is quite different from the harmonic wind stress profile that occurs in M1, and hence the surface Ekman transport structure differs greatly between the two solutions. Dispersion experiments with Lagrangian surface drifters in this experiment resulted in a dispersion power law behavior that is in very good agreement with available observations (Wolff and Bye 1998, manuscript submitted to *Ann. Glaciol.*).

The barotropic momentum balance of MCQS300 is, to a good degree, overshadowed by the boundary solutions in the lower layer, especially in combination with the strong anticyclonic circulation around Campbell Plateau (see Fig. 16b). This remarkable (and unrealistic) feature is created by a peculiarity of the evolving boundary layers as discussed in the appendix of Wolff et al. (1991) and the internal frictional constraints (zero bottom friction, zero explicit interfacial friction, and very small horizontal hyperviscosity). This leads to the remarkable effect that topographic form stress can be a strong source of westward momentum in order to counterbalance the Reynolds stress divergence of the standing eddy field in the vicinity of the Campbell Plateau. Ignoring the boundary layers, the overall momentum balance is close to the original experiment M1 in Wolff et al. (1991) but shows the distinct difference of the feedback to the atmospheric forcing. In this regard, even the layer transports are closer to observed values (130 to 140 Sv; Rintoul 1997, personal communication) than in the older experiment M1.

c. Flat bottom rectangular basin (DGS300)

For the rectangular basin, we will discuss only the 300-day current average solution (DGS300). The 30-day current average solution was close to a basin res-

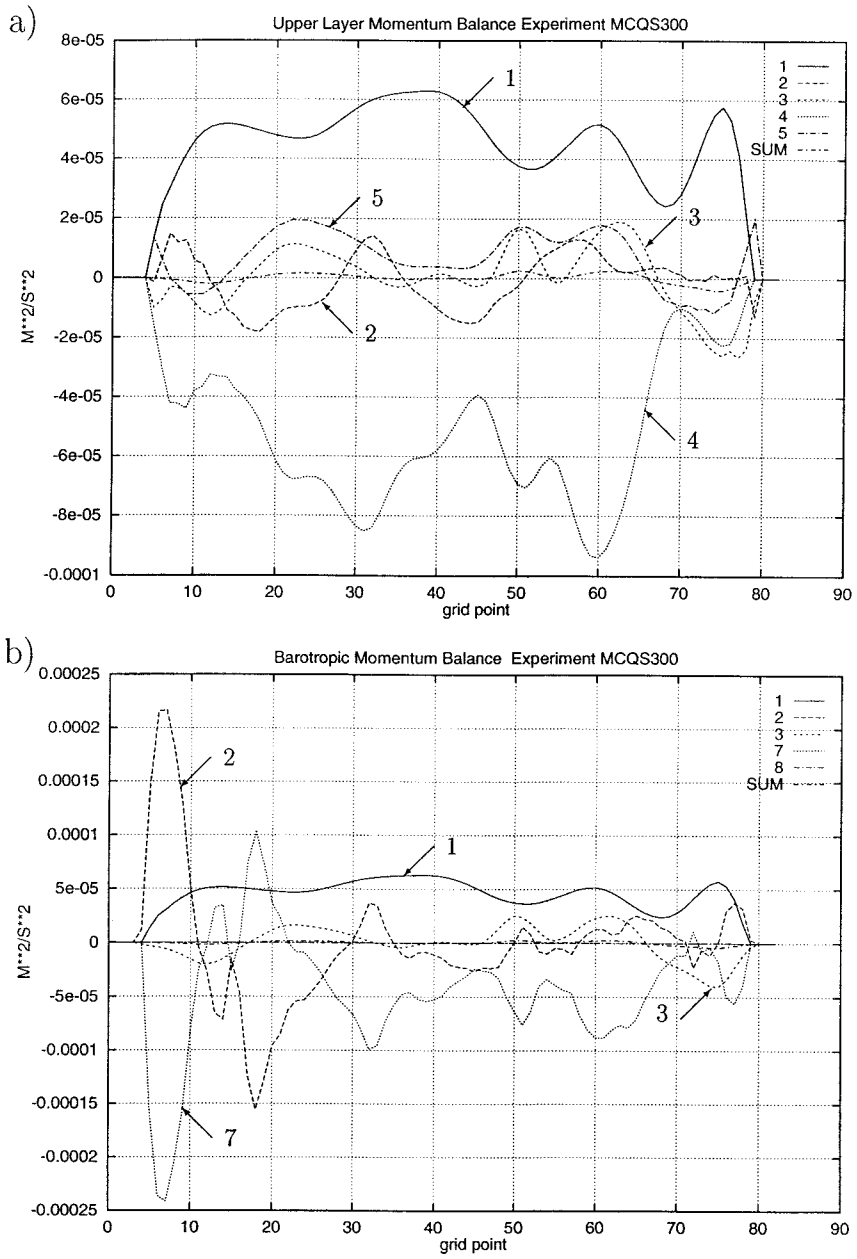

FIG. 21. Experiment MCQS300: (a) upper layer momentum balance and (b) barotropic momentum balance. Contributing terms are surface stress (1), Reynolds stress divergence of the standing eddies (2) and transient eddies (3), interfacial form drag due to standing eddies (4) and transient eddies (5), topographic form stress (7), and bottom friction (8). Lateral friction effects (6) are negligible and therefore not displayed. Units are $m^2\ s^{-2}$. The northern and southern boundaries are located at grid points 4 and 79, respectively.

onance for a barotropic Rossby wave, which would not appear to have any significance for a real ocean basin and is therefore not discussed in detail. The mean streamfield (Fig. 22) is of similar intensity to the I series solution; however, the retroflective streamline pattern, which disperses the central jet, has been smoothed by the eddy field, which also reduces the penetration of the jet into the basin (Fig. 22a). The lower layer (Fig. 22b) reflects the changes in the upper layer, in so far as the recirculating region contracts toward the western boundary, and the vorticity is more evenly distributed throughout the basin.

The instantaneous streamfield in the upper layer (Fig. 23a) shows a meandering jet that sheds both cyclonic and anticyclonic eddies. The general appearance of the streamfield is similar to that observed with bottom fric-

a)

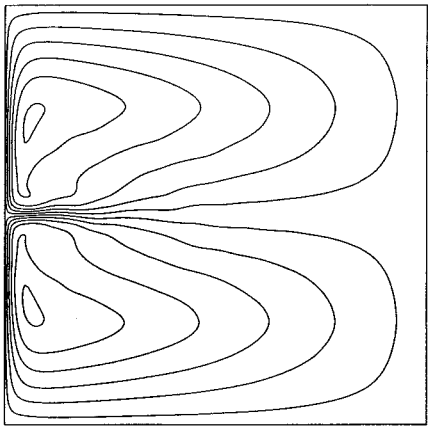

b)

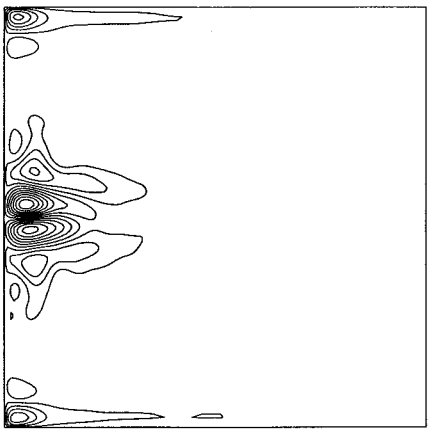

FIG. 22. Time-mean streamfunctions of experiment DGS300: (a) upper layer CI = 5×10^3 m^2 s^{-1} and (b) lower layer CI = 500 m^2 s^{-1}.

tion (Holland 1978). In the lower layer, the coherent trains of low intensity Rossby Waves that occur in the I series solution have been obliterated by a random eddy pattern of greater intensity (Fig. 23b).

The instantaneous reference streamfield (Fig. 24a) shows that the transient eddies are distributed throughout the basin. The instantaneous Stokes surface streamfunction (Fig. 24b) has a simple gyral pattern due to the smoothness of both the $\mathbf{u}_1(T_1)$ and $\mathbf{u}_2(T_2)$ fields (for a flat bottom ocean).

The instantaneous shear stress $\hat{\boldsymbol{\tau}}_{s0}$ shows a similar smooth field (Fig. 25b). The western boundary currents give rise to intense ''stress gyres'' of the same sign of rotation as the associated ocean gyre. The interesting feature here is that the Ekman transport due to the western boundary current has opposite signs for the two gyres. In the Gulf Stream gyre a downwelling frictional circulation occurs across the stream, whereas in the Labrador gyre an upwelling frictional circulation exists across the stream. The thermodynamics of these current-induced transverse frictional circulations have been discussed in Bye (1986).

Figure 25a shows the surface shear stress $\boldsymbol{\tau}_{s0}$, which occurs on the scale of the mesoscale eddies. The exchange of momentum with the atmosphere due to the eddies in the neighborhood of the central jet is clearly shown; however, in the interior of the ocean basins the field is almost independent of the ocean circulation.

The energy time series (Fig. 26) are similar to those from the I series solution (Fig. 13) and show the dominance of the potential energy P over the kinetic energy K_i of the two layers. The system rapidly settles down to a statistical equilibrium, but there is evidence of an energy cycle of about 300 days in P and K_1 of the upper layer. The lower layer K_2 displays a longer period variability of moderate intensity $\pm 15\%$.

d. Conclusion

The important conclusion from the S series solutions is that, as the current averaging period increases from 30 to 300 days, a vigorous field of transient eddies occurs. The reason for this behavior can be seen by assuming that $\mathbf{u}_2(T_2)$ and $\mathbf{u}_2$ are uncorrelated in (7), which then reduces to the approximate form,

$$\hat{\boldsymbol{\tau}}_{s0} \sim \rho_1 K_I \left| \mathbf{u}_1 - \frac{\mathbf{u}_2(T_2)}{\epsilon} \right| \left(\mathbf{u}_1 - \frac{\mathbf{u}_2(T_2)}{\epsilon} \right), \quad (17)$$

which is almost independent of the transient eddy field. In other words, the eddies are free to evolve independently and can become a fully developed component of the system. For the mesoscale eddies, $\boldsymbol{u}_2(T_2)$ and $\boldsymbol{u}_2$ become significantly decorrelated for timescales greater then the eddy timescale, and in the S series solutions the transition occurs between 30 and 300 days, with the progressive development of the eddy field. As the ocean general circulation responds to seasonal forcing, we conjecture that the current averaging period may have an upper bound, but this possibility has not been investigated.

7. Discussion

a. The basin-scale momentum balance

An important conclusion from the S series solutions is that the long-period current-averaged shear stress is of the form (17). This result indicates that $\hat{\boldsymbol{\tau}}_{s0}$, which determines the surface Ekman transport, is a quasi-steady field that is almost unperturbed by the mesoscale eddies. Also, $\boldsymbol{\tau}_{s0}$ determined from the I series solution is a quasi-steady field; see section 5. The difference between these two fields is due to the modulation of the mean velocity field by the transient eddies that are present in the solutions with current averaging but absent in the solutions with no current averaging. A comparison

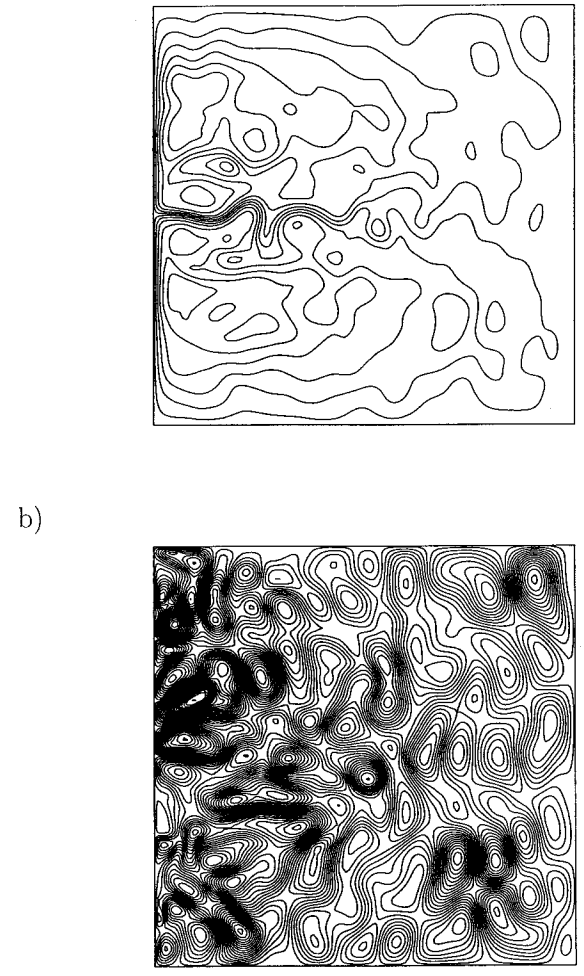

FIG. 23. Instantaneous streamfunctions of experiment DGS300: (a) upper layer CI = 5×10^3 m^2 s^{-1} and (b) lower layer CI = 500 m^2 s^{-1}.

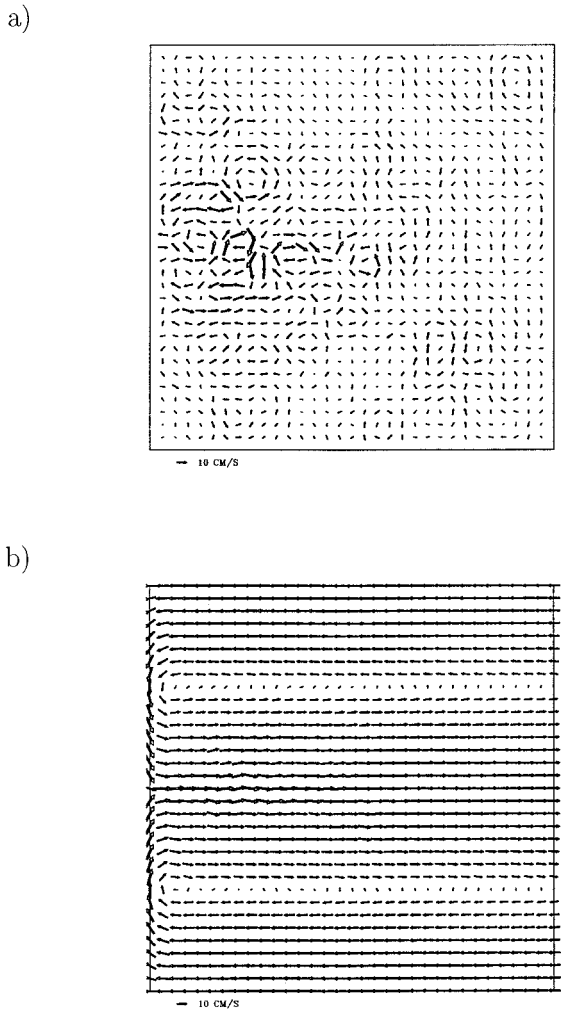

FIG. 24. Experiment DGS300: (a) reference velocity field and (b) Stokes drift.

between Figs. 7 and 16 and between Figs. 11 and 22 indicates that the differences in the streamfields are not great. The following conclusions can be drawn from this comparison:

1) The momentum balance for the mean ocean circulation is well represented using (17), which has the form of the original Stommel body friction model.
2) The Reynolds stress transfers that are the substance of the Munk lateral friction model are of lesser importance, and the streamfields indicate that the apparent coefficient of lateral viscosity may have either sign; for example, the greater dispersion of the midbasin jet in Fig. 22 relative to Fig. 11 indicates a positive coefficient, and the formation of a jet in the western channel in Fig. 16, which is absent in Fig. 7, indicates a negative coefficient.
3) The presence of the eddy field leads to the enhancement of the effect of the surface current in $\hat{\boldsymbol{\tau}}_{s0}$ as conjectured in Bye (1980).
4) The use of (8) in noneddy-resolving general circulation models may be expected to yield realistic mean circulation fields.

b. *The evolution of two-dimensional turbulence in coupled fluids*

The difference between $\boldsymbol{\tau}_{s0}$ and $\hat{\boldsymbol{\tau}}_{s0}$ can also be interpreted in terms of the theory of 2D turbulence. The $\hat{\boldsymbol{\tau}}_{s0}$ field pertains to the largest scale of motion, whereas $\boldsymbol{\tau}_{s0}$ applies on the scale of the mesoscale eddies, which is the smallest scale of resolution in the model. Thus the energy transfers that occur through the $\boldsymbol{\tau}_{s0}$ field are an internal energy flux of the 2D turbulence, which transfers energy to the lower wavenumbers. The transfer process occurs through the inertial coupling, in which there is no requirement for energy dissipation as is illustrated in the example in the appendix.

a)

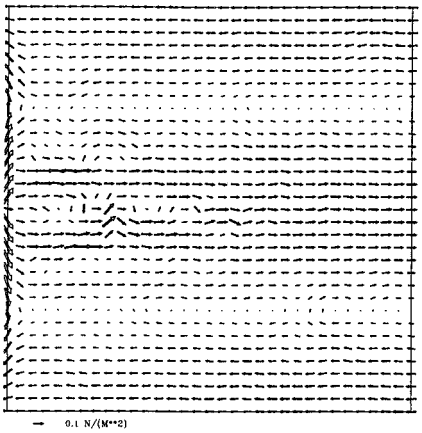

b)

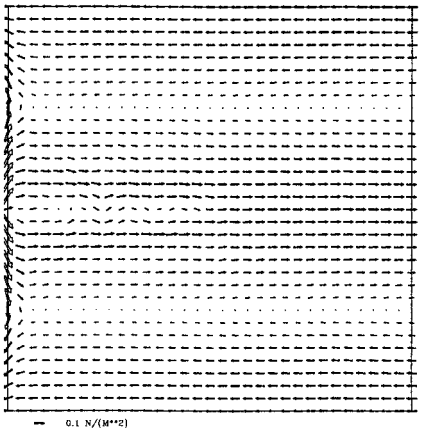

FIG. 25. Experiment DGS300: (a) $\boldsymbol{\tau}_{s0}$ and (b) $\hat{\boldsymbol{\tau}}_{s0}$.

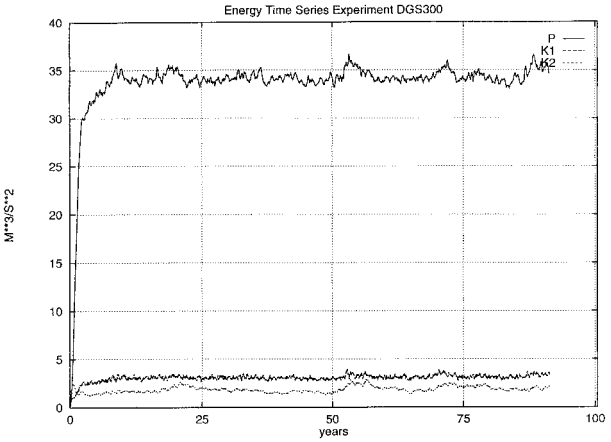

FIG. 26. Experiment DGS300: Time evolution of potential energy (P) and layer kinetic energies (K_1, K_2). Energy values in $m^3\,s^{-2}$. Time axis in units of years.

The low wavenumber limit is a portrait of the fluid as a 2D entity, whereas at higher wavenumbers the inner workings of the fluid are revealed through the inertial coupling process. At this level, all that is known is that there occurs an energy flux to the low wavenumbers, that is, out of the system. The fate of the energy flux is conditional: it may or may not cascade to lower wavenumbers. What actually happens is determined for the lower fluid by the upper fluid.

In the example in the appendix, it is assumed that there is no dissipation, and hence the flux E_2 is passed on unchanged to lower wavenumbers. The magnitude of E_2 is maximized for $\epsilon \to 0$, that is, in which the energy of the upper fluid is negligible. This response is the classical energy cascade discussed by Kraichnan (1967).

The coupled fluids, however, may choose a completely different mutual response. Let us suppose that there is no surface wind ($\mathbf{u}_1 = 0$) and also that there is no mean current ($\mathbf{u}_2(T_2) = \overline{\mathbf{u}}_2 = 0$) but only an oscillatory tidal current ($\mathbf{u}_2$). Then, from (5) $\boldsymbol{u}_L = 0$ and from (6) $\mathbf{u}_0 = \mathbf{u}_2/(1 + \epsilon)$ and on substituting in (7), we have

$$\hat{\boldsymbol{\tau}}_{s0} = \boldsymbol{\tau}_s = \frac{-\rho_1 K}{(1+\epsilon)^2}|\mathbf{u}_2|\mathbf{u}_2. \tag{18}$$

This situation corresponds to a simple (viscous) dissipation in which all the energy flux entering the wave boundary layer is dissipated locally and no energy cascade occurs.

In general, the response lies between the above two extremes and cannot be determined without reference to the 2D turbulence occurring in both the upper and lower fluids.

For the oceanic general circulation that we have considered, in which $\mathbf{u}_1(T_1) = \mathbf{u}_1$, the instantaneous downward energy fluxes in the air and water are, respectively, $\hat{E}_1 = \hat{\boldsymbol{\tau}}_{s0} \cdot \mathbf{u}_1$ and $\hat{E}_2 = \hat{\boldsymbol{\tau}}_{s0} \cdot \mathbf{u}_2$, from which on substituting (7) in $\hat{E}_1$, we obtain

$$\hat{E}_1 = \rho_1 K_1 \left| \mathbf{u}_1 - \frac{1}{\epsilon}\mathbf{u}_2(T_2) - \frac{2(\mathbf{u}_2 - \mathbf{u}_2(T_2))}{1+\epsilon} \right| \times \left(\mathbf{u}_1^2 - \frac{1}{\epsilon}\mathbf{u}_2(T_2)\cdot\mathbf{u}_1 - \frac{2(\mathbf{u}_2 - \mathbf{u}_2(T_2))}{1+\epsilon}\cdot\mathbf{u}_1 \right). \tag{19}$$

Here, $\hat{E}_1$ is the sum of three processes: (i) dissipation in the wave boundary layer $\sim\mathbf{u}_1^2$, (ii) energy transfer by the mesoscale eddies, which in the mean is very small, and (iii) if $\mathbf{u}_2(T_2) \cdot \boldsymbol{u}_1 > 0$, an upward transfer of energy from the ocean to the atmosphere. This latter term is the sink of energy for the 2D turbulence of the oceanic general circulation, through which the low wavenumber limit can be said to radiate its energy away into the atmosphere. In effect, it is the aura of the denser fluid.

c. The wave model

The accuracy of the method of solution is limited by the precision of the procedure used to compute $\mathbf{u}_L$ in (5). We have used simple moving averages to calculate the effective wind and current velocities that generate the surface Stokes drift, in which the only two parameters are their respective lengths, T_1 and T_2. For a time varying wind, T_1 could be chosen to simulate the response to synoptic atmospheric systems; for example, $T_1 \sim 10$ h. A more sophisticated treatment would use a spectral wave model to estimate $\mathbf{u}_L$.

8. Conclusions

We have reexamined the formulation of the surface shear stress applicable to general circulation modeling. The main conclusion is that the shear stress depends on the specification of the reference frame used in its evaluation. Thus, it is important to identify the reference frame in the definition. In this paper, we use $\boldsymbol{\tau}_s$ with reference to the expression (2), which involves the surface reference velocity $\mathbf{u}_0$ and is applicable for planetary boundary observations, and distinguish the shear stress in the earth reference frame by $\boldsymbol{\tau}_{s0}$. In this context, three significant conclusions may be stated:

1) The planetary boundary layer measurements are made in a noninertial frame. Hence their interpretation in terms of momentum transfer across the sea surface is highly misleading. The implementation of (2) ''relative to the surface current,'' that is, with $\mathbf{u}_0 \sim \mathbf{u}_2$, is not justified for estimating momentum transfer; see section 3.
2) In the earth reference frame, the shear stress relation depends on the scale of averaging of the motion in the atmosphere and ocean. In the numerical experiments, $\boldsymbol{\tau}_{s0}$ refers to the shear stress on the smallest timescale of resolution of the model and $\hat{\boldsymbol{\tau}}_{s0}$ refers to the largest timescale, which is the current averaging period. Both these fields are instantaneous fields; see section 3b; thus, by inference the shear stress at the sea surface is also a function of the averaging period. This result is well known for $\boldsymbol{\tau}_s$, where the Reynolds stress is computed from fluctuations over a specified time period. Our analysis extends the averaging concept to include horizontal eddy motions.
3) The I series solutions suggest that (8) is a realistic boundary condition to be applied in noneddy-resolving (climate) models, and the S series solutions suggest that (7) would be appropriate for eddy-resolving general circulation models with $T_1 \sim 10$ h and $T_2 \sim 100$ days. These conjectures remain to be tested.

The solutions obtained for the channel with topography and also the flat bottom rectangular basin show that the application of the surface shear stress $\hat{\boldsymbol{\tau}}_{s0}$ leads to momentum balances broadly consistent with observations, without the need for a large (unrealistic) bottom friction.

Acknowledgments. We would like to thank Dr Nathan Bindoff for fruitful and inspiring discussions on the subject of vertical momentum fluxes between atmosphere and ocean. Helpful comments by the referees are also gratefully acknowledged.

APPENDIX

The Dependence of the Surface Shear Stress on the Reference Frame

The answer to the question, whether the surface shear stress measured in the local coordinate system and in the reference frame of the solid body rotation of the earth is identical, takes us to the center of fluid dynamics, at which level the equations of motion are formulated.

a. The equation of motion on a shaky plane

The inertial coupling relation (2a) indicates that at the sea surface there exists a local reference velocity field $\mathbf{u}_0(x, y, t)$ in the expression for the surface shear stress. The surface boundary is, in fact, made up of a mosaic of horizontal perturbation velocities, through which the vertical momentum transfers occur, and which may be aptly described as a ''shaky plane.'' The large-scale horizontal motions, however, are embedded in a rigid container. In the transfer of momentum between the vertical and the horizontal, account must be taken of this difference in reference.

b. Multiple reference frames

The resolution of the problem discussed in section a is to suppose that the frictional stress in the fluid causes accelerations relative to a velocity $\mathbf{u}_N$. According to this hypothesis, the equations of motion of the fluid, to the Boussinesq approximation are

$$\frac{\partial}{\partial t}(\mathbf{u} - \mathbf{u}_N) + \mathbf{u} \cdot \frac{\partial}{\partial \mathbf{x}}(\mathbf{u} - \mathbf{u}_N) + \left[\frac{\partial}{\partial t}\mathbf{u}_N + \mathbf{u} \cdot \frac{\partial}{\partial \mathbf{x}}\mathbf{u}_N + \mathbf{f} \times \mathbf{u}\right] = -\frac{1}{\rho_0}\frac{\partial p}{\partial \mathbf{x}} + F(\mathbf{u} - \mathbf{u}_N) + \frac{\rho}{\rho_0}\mathbf{g}, \qquad \text{(A1)}$$

where $\mathbf{f} = 2\Omega \sin\Phi\mathbf{k}$ in which $\mathbf{k}$ is vertically upward, Ω is the angular speed of rotation of the earth, Φ is latitude, p is pressure, $\mathbf{g} = -g\mathbf{k}$ where g is the acceleration of gravity, $F(\mathbf{u} - \mathbf{u}_N)$ is the frictional force acting in the fluid, and ρ and ρ_0 are, respectively, the density and a standard density. In (A1), the term in square brackets is the material rate of change of the reference velocity $\mathbf{u}_N$. This consists of two parts: (i) the Coriolis acceleration due to the rotation of the rigid container and (ii) a local acceleration due to the change in reference velocity of the fluid within the rigid container.

The important difference between (A1) and the Navier–Stokes equation is that the frictional forces are defined relative to $\mathbf{u}_N$. There are three ''natural'' choices for $\mathbf{u}_N$, which enable fluid behavior to be studied. We consider each in turn.

1) THE INTERNAL REFERENCE FRAME

Consider conditions within the fluid and assume that (2) can be applied at any level (z), and that the fluid density and velocity vary in the vertical. From (2a) we obtain, for a wave boundary layer ($z + z_B \geq z \geq z - z_B$),

$$\boldsymbol{\tau}_z = \frac{1}{4}K\rho\left|(\mathbf{u}_1 - \mathbf{u}_2) + \frac{1}{2}\frac{(\rho_1 - \rho_2)}{\rho}(\mathbf{u} - \mathbf{u}_N)\right|\left((\mathbf{u}_1 - \mathbf{u}_2) + \frac{1}{2}\frac{(\rho_1 - \rho_2)}{\rho}(\mathbf{u} - \mathbf{u}_N)\right) + O\left(\frac{\rho_1 - \rho_2}{\rho}\right)^2, \quad \text{(A2)}$$

in which $\rho = (\rho_1 + \rho_2)/2$ and $\mathbf{u} = (\mathbf{u}_1 + \mathbf{u}_2)/2$ are the density and velocity, and $\boldsymbol{\tau}_z$ is the shear stress. On considering the limit in which the wave boundary layer thickness, $2z_B \to 0$, which is the internal reference frame for the fluid, (A2) yields

$$\boldsymbol{\tau}_z = \eta\frac{\partial}{\partial z}[\sqrt{\rho}(\mathbf{u} - \mathbf{u}_N)], \quad \text{(A3)}$$

where

$$\eta = K\left|\frac{\partial}{\partial z}[\sqrt{\rho}(\mathbf{u} - \mathbf{u}_N)]\right|z_B^2$$

is a coefficient of viscosity.

To the Boussinesq approximation for the square root of density, (A3) reduces to the relation,

$$\boldsymbol{\tau}_z = \rho A\frac{\partial(\mathbf{u} - \mathbf{u}_N)}{\partial z}, \quad \text{(A4)}$$

in which

$$A = K\left|\frac{\partial \mathbf{u}}{\partial z}\right|z_B^2$$

is a coefficient of dynamic viscosity. Equation (A4) is of Newtonian form in which $\boldsymbol{\tau}_z$ is proportional to the velocity shear.

In the limit ($2z_B \to 0$), (2b) yields

$$\mathbf{u} - \mathbf{u}_N = \mathbf{u}_L + O\left(\frac{\rho_1 - \rho_2}{\rho}\right), \quad \text{(A5)}$$

an axiomatic equation, which states that the fluid velocity $\mathbf{u}$ relative to the reference velocity $\mathbf{u}_N$ is the inertial velocity $\mathbf{u}_L$.

2) THE SURFACE REFERENCE FRAME

In the surface reference frame,

$$\mathbf{u}_N(x, y, z, t) = \mathbf{u}_0(x, y, t). \quad \text{(A6)}$$

The horizontal scale of variability of $\mathbf{u}_0$ in a steady circulation pattern in both fluids is determined by changes in the wavefield $\mathbf{u}_L$ and in the open ocean it is determined by the synoptic scales of the atmosphere and the ocean. This scale normally would be much larger than the ocean depth, so that the horizontal dynamics are almost uniform. This situation can be used to define a surface reference frame.

For this reference frame to have any utility, it is assumed that along the vertical, $\mathbf{u}_N = \mathbf{u}_0$. This uniformity in the vertical is also an approximation as, in general, relative motion exists between the interface and the bottom (or top) boundary due to the shaky plane, but over a small distance in either fluid, compared with its vertical extent, it is likely to be a good approximation. In the limit of horizontally homogeneous conditions and two fluids of infinite extent, $\mathbf{u}_N$ tends to a constant velocity in a small domain adjacent to the interface in which the frictional term is $F(\mathbf{u} - \mathbf{u}_N)$. This situation defines the planetary boundary layer reference frame. Since regions always exist in which $\mathbf{u}_N$ changes, either spatially or temporally, this reference frame is necessarily an incomplete framework with which to describe the physics of the fluid.

3) THE EARTH REFERENCE FRAME

In the reference frame of the container (the earth reference frame),

$$\mathbf{u}_N(x, y, z, t) = 0 \quad \text{(A7)}$$

and the frictional term differs crucially from that in reference frame 2, and is of the form $F(\mathbf{u})$. In particular the surface shear stress, given by the inertial coupling relation, is

$$\boldsymbol{\tau}_{s0} = K_I|\rho_1^{1/2}\mathbf{u}_1 - \rho_2^{1/2}\mathbf{u}_2| \times (\rho_1^{1/2}\mathbf{u}_1 - \rho_2^{1/2}\mathbf{u}_2), \quad \text{(A8)}$$

where $K_I = \frac{1}{4}K_0(\pm z_B)$ and $\boldsymbol{\tau}_{s0}$ and K_0 are applicable for $\mathbf{u}_0 = 0$. This formulation applied at the position (x, y) on the sea surface at time (t) has no direct relation with the local surface shear stress actually measured in the boundary layer, which is given by (2a). This framework is used implicitly in general circulation modelling for which (A8) provides a surface boundary condition. Equation (A8) is an *active no slip* condition in which

the tangential velocity on the boundary is zero ($\mathbf{u}_0 = 0$) and the tangential stress is specified by the velocities in the fluids on *both* sides of the interface.

c. Vertical energy transfer across the sea surface

The implications of the existence of the two reference frames 2 and 3 are profound and can be illustrated by the analysis of the energetics of a current. Let us suppose that the interfacial dissipation of energy due to the current is negligible. In this situation, the velocity shear between the air and water induced by the circulation would be negligible. Hence in the surface reference frame, $\mathbf{u}_1 = \mathbf{u}_2 = \mathbf{u}_0$, such that $\boldsymbol{\tau}_s = 0$ and no account need be taken of the existence of $\mathbf{u}_2$. The usual argument, which is advanced to justify this result is that the selection of the reference frame is arbitrary in classical (Newtonian) dynamics, and hence the solution must be independent of $\mathbf{u}_2$. This proposition however is unsafe as the problem is being considered in the surface reference frame, which is not a Newtonian reference frame.

In the earth reference frame, which is Newtonian, we conclude differently. Consider the vertical energy fluxes through the interfacial boundary layer. Across the edge of the constant stress boundary layer in the water, the downward energy flux,

$$E_2 = \boldsymbol{\tau}_{s0} \cdot \mathbf{u}_2, \tag{A9}$$

where

$$\boldsymbol{\tau}_{s0} = K_I|(\sqrt{\rho_1} - \sqrt{\rho_2})\mathbf{u}_2| \times (\sqrt{\rho_1} - \sqrt{\rho_2})\mathbf{u}_2$$

is negative ($E_2 \leq 0$). The corresponding downward energy fluxes across the sea surface and into the constant stress layer in the air are, respectively,

$$E_0 = \boldsymbol{\tau}_{s0} \cdot \mathbf{u}_0 \tag{A10}$$

and

$$E_1 = \boldsymbol{\tau}_{s0} \cdot \mathbf{u}_1. \tag{A11}$$

Since $\mathbf{u}_1 = \mathbf{u}_0 = \mathbf{u}_2$, we obtain

$$E_1 = E_0 = E_2. \tag{A12}$$

In other words, in the earth reference frame, with no shear between the free stream velocities $\mathbf{u}_1$ and $\mathbf{u}_2$, there occurs an innate *upward* energy transfer from the ocean to the atmosphere due to the current; see section 7b. This interfacial energy loss process is also a constituent part of the energy transfer in the more general situation in which $\mathbf{u}_1 \neq \mathbf{u}_2$.

REFERENCES

Abramowitz, M., and I. A. Stegun, Eds., 1972: *Handbook of Mathematical Functions.* 9th ed. Dover, 1046 pp.

Bye, J. A. T., 1980: Energy dissipation by the large scale circulations. *Ocean Modelling,* (unpublished manuscript) **31,** 12–13.

——, 1986: Momentum and heat balances in steady coastal currents. *Estuarine, Coastal, Shelf Sci.,* **23,** 1–28.

——, 1988: The coupling of wave drift and wind velocity profiles. *J. Mar. Res.,* **46,** 457–472.

——, 1995: Inertial coupling of fluids with large density contrast. *Phys. Lett. A,* **202,** 222–224.

——, 1996: Coupling ocean–atmosphere models. *Earth-Sci. Rev.,* **40,** 149–162.

——, and J.-O. Wolff, 1997: A quasi-geostrophic model of the Antarctic Circumpolar Current with inertial coupling. *Proc. Southern Ocean Workshop,* Adelaide, Australia, 1–7.

Chalikov, D. V., and V. K. Makin, 1991: Models of the wave boundary layer. *Bound.-Layer Meteor.,* **56,** 83–99.

Doyle, J. D., 1994: Air–sea interaction during marine cyclogenesis. *Proc. Conf. on Life Cycles of Extratropical Cyclones,* Vol. 3, Bergen, Norway, 61–66.

Ekman, V. W., 1905: On the influence of the Earth's rotation on ocean-currents. *Ark. Mat. Astron. Fys.,* **2** (11), 1–53.

Holland, W. R., 1978: The role of mesoscale eddies in the general circulation of the ocean—Numerical experiments using a wind-driven quasi-geostrophic model. *J. Phys. Oceanogr.,* **8,** 363–392.

——, and W. J. Schmitz, 1985: Zonal penetration scale of model midlatitude jets. *J. Phys. Oceanogr.,* **15,** 1859–1875.

Holloway, G., 1987: Systematic forcing of large-scale geophysical flows by eddy–topography interaction, *J. Fluid Mech.,* **184,** 465–476.

IPCC, 1995: *Climate Change 1995: The Science of Climate Change.* Contribution of Working Group I to the Second Assessment Report of the Intergovernmental Panel on Climate Change, ''Technical Summary'', J. T. Houghton, L. G. Meira Filho, B. A. Callander, N. Harris, A. Kattenberg, and K. Maskell, Eds., Cambridge University Press, 9–50.

Ivchenko, V. O., K. Richards, B. Sinha, and J.-O. Wolff, 1997: Parameterization of mesoscale eddy-fluxes in zonal flow of the ocean. *J. Mar. Res.,* **55**(6), 1127–1162.

Janssen, P. A. E. M., 1989: Wave-induced stress and the drag of airflow over sea waves. *J. Phys. Oceanogr.,* **19,** 745–754.

——, 1991: Quasi-linear theory of wind-wave generation applied to wave forecasting. *J. Phys. Oceanogr.,* **21,** 1631–1642.

——, 1992: Experimental evidence of the effect of surface waves on the airflow. *J. Phys. Oceanogr.,* **22,** 1600–1604.

——, and P. Viterbo, 1996: Ocean waves and the atmospheric climate. *J. Climate,* **9,** 1269–1287.

Jones, I. S. F., and Y. Toba, 1999: Wind stress over the ocean. Cambridge University Press, in press.

Kamenkovich, V. M., M. N. Koshlyakov, and A. S. Monin, 1986: Synoptic Eddies in the Ocean. D. Reidel, 433 pp.

Kenyon, K. E., 1969: Stokes drift for random gravity waves. *J. Geophys. Res.,* **74,** 6991–6994.

Komen, G. J., and L. Cavaleri, M. Donelan, K. Hasselmann, S. Hasselmann, and P. A. E. M. Janssen, 1994: *Dynamics and Modelling of Ocean Waves.* Cambridge University Press, 532 pp.

Kraichnan, R. H., 1967: Inertial ranges in two-dimensional turbulence. *Phys. Fluids,* **10,** 1417–1423.

Marshall, J. C., A. J. G. Nurser, and R. Brugge, 1988: On the time-averaged flow of quasi-geostrophic wind-driven gyres. *J. Geophys. Res.,* **93,** 15 427–15 436.

McWilliams, J. C., 1977: A note on a consistent quasigeostrophic model in a multiply connected domain. *Dyn. Atmos. Oceans,* **1,** 427–441.

——, W. R. Holland, and J. H. S. Chow, 1978: A description of numerical Antarctic Circumpolar Currents. *Dyn. Atmos. Oceans,* **2,** 213–291.

Munk, W. H., and E. Palmén, 1951: Note on the dynamics of the Antarctic Circumpolar Current. *Tellus,* **3,** 53–55.

Olbers, D. J., J.-O. Wolff, and C. Völker, 1999: Eddy fluxes and second-order moment balances for nonhomogenous quasigeostrophic turbulence in wind-driven zonal flows. *J. Phys. Oceanogr.,* in press.

Reynolds, O., 1894: On the dynamical theory of incompressible viscous fluids and the determination of the criterion. *Philos. Trans. Roy. Soc. London. A,* **186,** 123–164.

Rhines, P. B., and W. R. Young, 1982: Homogenization of potential vorticity in planetary gyres. *J. Fluid Mech.*, **122,** 347–367.
Veronis, G., 1996: Effect of a constant, zonal wind on wind-driven ocean circulation. *J. Phys. Oceanogr.*, **26,** 2525–2528.
Weber, S., 1994: Statistics of the air–sea fluxes of momentum and mechanical energy in a coupled wave–atmosphere model. *J. Phys. Oceanogr.*, **24,** 1388–1398.
Wolff, J.-O., 1990: Zur Dynamik des Antarktischen Zirkumpolarstromes. Dissertation am Fachbereich Geowissenschaften der Universität Hamburg, Examensarbeit Nr. 2 (PhD thesis), Max-Planck-Institut für Meteorologie, 142 pp.
——, and J. A. T. Bye, 1996: Inertial surface stress coupling in a two-layer quasi-geostrophic channel model. *Ocean Modelling* (unpublished manuscript), **112,** 6–8.
——, E. Maier-Reimer, and D. J. Olbers, 1991: Wind-driven flow over topography in a zonal β-plane channel: A quasi-geostrophic model of the Antarctic Circumpolar Current. *J. Phys. Oceanogr.*, **21,** 236–264.
——, A. V. Klepikov, and D. J. Olbers, 1993: On the eddy-potential-enstrophy balance in a two-layer quasi-geostrophic channel model. *Ocean Modelling* (unpublished manuscript), **101,** 2–5.